Sarah Laura Eisbacher, BSc

Synthesis and Characterization of Sulfide-Solid-Electrolytes

MASTER'S THESIS
to achieve the university degree of
Diplom-Ingenieurin

Master's degree programme: Technical Chemistry

submitted to
Graz University of Technology

Supervisors:
Univ.-Prof. Dr.rer.nat.habil. Martin Wilkening
Mag.rer.nat Dr.techn. Daniel Rettenwander

Institute for Chemistry and Technology of Materials

Graz, January 2019

Affidavit

I declare that I have authored this thesis independently, that I have not used other than the declared sources/resources, and that I have explicitly indicated all material which has been quoted either literally or by content from the sources used. The text document uploaded to TUGRAZonline is identical to the present master's thesis.

Graz, 03.01.2019

Eisbacher Sarah Laura

Acknowledgments

In the first place I want to thank my supervisors Univ.-Prof. Dr.rer.nat. Martin Wilkening and Mag.rer.nat. Dr.techn. Daniel Rettenwander of the Institute for Chemistry and Technology of Materials at Graz University of Technology for their help and input to this thesis.

Special thanks to Dipl.-Ing. Isabel Hanghofer for the great support. The door to Isabel's office was always open whenever I ran into a trouble spot or had a question about my research.

Moreover I want to thank Dipl.-Ing. Dr. techn. Brigitte Bitschnau and Ao.Univ.-Prof. Dipl.-Ing. Dr. techn. Franz-Andreas Mautner for the numerous XRD-measurements and the help with the interpretation of my results.

Special thanks to the whole AGW for the nice working atmosphere and any kind of help.

Furthermore, I want to acknowledge the Christian Doppler Laboratory for Lithium-Ion-Batteries for the financial support.

A very special thank to the best fellow students, Verena and Paul. Thank you for listening, offering me advice and supporting me, whenever I needed you.

Finally, I must express my very profound gratitude to my parents, Silvia and Hubert, and my sister, Ina-Maria, for providing me with unfailing support and continuous encouragement throughout my years of study and through the process of researching and writing this thesis. This accomplishment would not have been possible without you. Thank you!

Abstract

Lithium-ion batteries are considered as leading electrochemical storage technology for successful realization of renewable energy.

Due to its simple design and long lifetime solid state lithium-ion batteries are attractive energy sources for many electrochemical applications. Large-scale lithium-ion batteries are developed for applications in automotive propulsion and stationary load-leveling for power generation (e.g. wind or solar energy).

The key material for realization of solid state lithium-ion batteries is a successful solid electrolyte. Compared to conventional organic liquid electrolytes solid electrolytes are safer, due to non-flammability with no liquid leakage. Sulfide solid electrolytes can reach a conductivities of 10^{-2} $S \cdot cm^{-1}$ at room temperature. This value is as high as conductivities reached in organic liquid electrolytes. Therefore inorganic solid electrolytes with Li^+ ion conductivity were developed. [1]

The aim of this master's thesis was the synthesis and electrochemical characterization of various sulfide solid electrolytes. Lithium argyrodites based on the chemical formula Li_6PS_5X (X: F, Cl, Br and I) and antiperovskites based on the chemical formula A_3SI (A: Ag and Li) were prepared and characterized. The reactions were carried out by solid state reaction. The structures of those materials were characterized via X-ray powder diffraction. In order to determine transport properties solid-state impedance spectroscopy was used to study ion dynamics of the samples prepared.

Kurzfassung

Lithium-Ionen-Batterien werden als führende elektrochemische Speichertechnologien für die erfolgreiche Realisierung erneuerbarer Energien angesehen.

Aufgrund ihres einfachen Designs und ihrer langen Lebensdauer stellen Festkörper-Lithium-Ionen-Batterien für viele elektrochemische Anwendungen attraktive Energiequellen dar. Großtechnisch werden Lithium-Ionen-Batterien für Anwendungen im Automobilantrieb aber auch zur stationären Lastnivellierung für die Stromerzeugung (z.B. aus Wind- oder Solarenergie) entwickelt.

Die Schlüsselkomponente für die Realisierung von Festkörper-Lithium-Ionen-Batterien ist der Festelektrolyt. Im Vergleich zu herkömmlichen organischen Flüssigelektrolyten sind Festelektrolyte sicherer, da sie nicht entflammbar sind. Sulfidische Festelektrolyte können bei Raumtemperatur Leitfähigkeiten von 10^{-2} $S \cdot cm^{-1}$ erreichen. Dieser Wert entspricht den Leitfähigkeiten organischer flüssiger Elektrolyte. Daher wurden anorganische Festelektrolyte mit Li^+ -Ionenleitfähigkeit entwickelt.

Ziele dieser Masterarbeit waren die Synthese und elektrochemische Charakterisierung verschiedener sulfidischer Festkörperelektrolyte. Lithium-Argyrodite, basierend auf der chemischen Formel Li_6PS_5X (X: F, Cl, Br und I) und Antiperovskite gemäß der Summenformeln A_3SI (A: Ag, Li) wurden hergestellt und charakterisiert. Die Herstellung erfolgte mittels Festkörpersynthese und wurde mit Hilfe von Pulverröntgendiffraktometrie überprüft.

Content

Abbreviations

AC	Alternating Current
DC	Direct Current
EIS	Electrochemical impedance spectroscopy
ICSD	Inorganic Crystal Structure Database
SEM	Scanning Electron Microscopy
XRPD	X-ray powder diffraction

1 Introduction

In context to this master's thesis the theoretical background is described in the first part. Based on theoretical fundamentals the synthesis route is carried out successfully through solid-state reaction, where the second part is devoted to. For electrochemical characterization the prepared sulfide ionic conductors are evaluated with the help of X-ray powder diffraction and impedance spectroscopy, which is discussed in the third part of this thesis. In the last part, the conclusion, the results are summarized.

1.1 Motivation

Since ion conductors represent one of the most important material groups in electrochemical application, the improvement of its properties, as well as the preparation and characterization of new compounds is constantly being researched.

The aim of this master's thesis was the synthesis and characterization of sulfide ionic conductors with varying stoichiometry according to the lithium argyrodite Li_6PS_5X (X: Cl, Br, I, F) and antiperovskites A_3SI (A: Ag and Li).

In order to be able to define the structure and the crystallographic properties of the ion conductors, X-ray powder diffraction was carried out. With the help of X-ray diffraction, the solid state reaction and the stability of the samples could also be investigated.

Subsequently, impedance spectroscopy was performed to determine processes occurring within the solid-state electrolyte.

1.2 Sulfide ionic conductors

Lithium ion batteries with an inorganic solid electrolyte have some advantages over those with an organic liquid electrolyte. Inorganic solid electrolytes are safer and more reliable. The battery design is simplified, which leads to an improved safety and a longer durability. [2]

Sulfide solid electrolytes with a Li^+-ion conductivity have attracted much attention because of good mechanical properties, such as elastic modulus as well as process-ability. Sulfide solid electrolytes also show a better formability than oxide electrolytes. But there is also a shortcoming in case of chemical stability of sulfide solid electrolytes. In air atmosphere this type of electrolyte is not stable, because sulfides tend to decomposition by hydrolysis, forming hydrogen sulfide, H_2S, which is harmful. Therefore it is important to avoid contamination with air atmosphere. [1]

1.3 Solid state reaction

A common method to synthesize polycrystalline solids is the mixture of starting materials in the solid state as a direct reaction via ball milling. In comparison to conventional wet-chemical synthesis, this method is characterized by its simplicity in sample preparation and handling. [3, 4]

In Figure 1 the working principle of a ball milling process is shown.

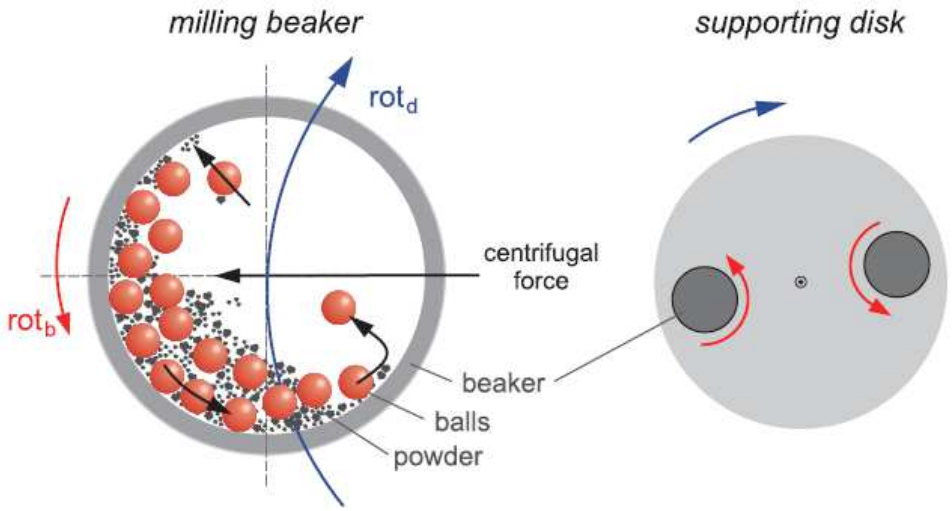

Figure 1[1]: Working principle of a ball milling process. The grinding beakers are filled with educts and ZrO_2-balls with a diameter of 5 mm. The beakers are arranged on a rotating supporting disk and a special mechanism causes them to rotate around their own axes. The centrifugal force produced by the vials and the rotating supporting disk act on the vials content.

Another important process of solid state reaction is the solid state sintering. Solid state sintering leads to a densification of particles via heat treatment below the melting point of the material. The rate of sintering is determined by three main factors: temperature and pressure, which control the diffusion rate and the particle size of the powder. The latter one controls the length scale for diffusion. [5]

In this work both processes, ball milling as well as solid state sintering, were used for sample preparation.

[1] *M. Wilkening, A. Duevel, F. Preishuber-Pflügl, K. Silva, S. Breuer, V. Sepelak, P. Z. Kristallogr. 2016,* ***2016***

2 Fundamentals

This chapter gives an insight into the theoretical background of solid-state chemistry including the topics diffusion of solids and defects in crystals. Furthermore X-ray powder diffraction and impedance spectroscopy are discussed in more detail.

2.1 Diffusion in solids

Diffusion in solids presents the movement of ions in a solid crystal lattice. During an ionic diffusion process, an atom diffuses out of its regular place in the lattice by making a series of elementary jumps to the nearest vacancy or interstitial positions. With the help of Fick's first law (Equation 2.1), it is possible to describe this ionic diffusion process macroscopically. [6]

First Fick's law:

$$\vec{j} = -D^{tr}\nabla c \tag{2.1}$$

Here $\vec{j}$ describes the particle's flux and D^{tr} the tracer diffusion coefficient. ∇c represents the concentration gradient [6]. With a constant particle number the following equation 2.2 is valid: [7]

$$-\nabla\vec{j} = \frac{\partial c}{\partial t} \tag{2.2}$$

The diffusion equation can be obtained by inserting equation 2.1 in equation 2.2 and is known as the second Fick's law (Equation 2.3) [7].

Second Fick's law:

$$\frac{\partial c}{\partial t} = \nabla(D^{tr}\nabla c) \tag{2.3}$$

For an elementary jump, like it is described in equation 2.1, an atom that jumps to a neighboring site in the lattice needs energy, because it needs to "pinch" through the lattice atoms. Such an atomic jump is described in the following equation 2.4.

$$G^M = H^M - TS^M \tag{2.4}$$

H^M describes the enthalpy and S^M the entropy of migration. T is the temperature and G^M denotes the Gibb's free energy of migration [7].

In Figure 2 the free energy activation is shown.

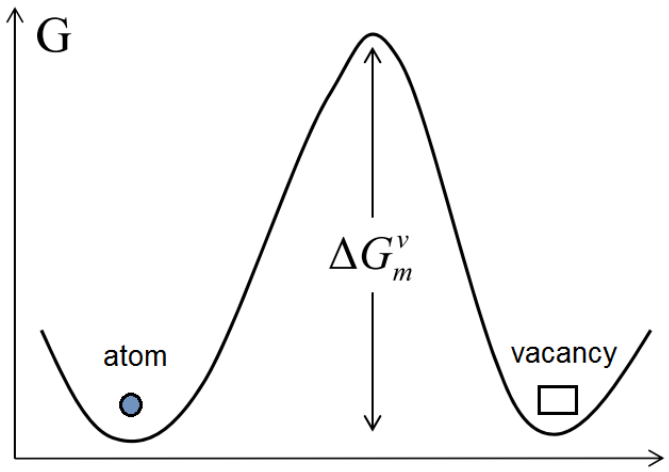

Figure 2: Free energy activation ΔG_m^v is the difference between the ground state and the saddle point.

Thermally activated motion of jumping ions in a crystal lattice occurs in a series of discrete jumps from one site to another. For this temperature-dependant diffusion coefficient D^{tr}, the Arrhenius relationship (Equation 2.5) is accurate:

$$D^{tr} = D_0^{tr} \exp\left(-\frac{E_A}{kT}\right) \tag{2.5}$$

Here E_A is the activation energy, k the Boltzmann constant and D_0^{tr} the pre-exponential factor [7].

A fundamental relation for impedance spectroscopy, which is important for this work, is the Nernst-Einstein-relation. In this relation, the charge diffusion coefficient D^{σ} is defined as followed:

$$\mathrm{D}^{\sigma} = \frac{\sigma_{\mathrm{DC}}\,\mathrm{k\,T}}{\mathrm{N\,q}^2} \tag{2.6}$$

σ_{DC} is the direct current ion conductivity, k and T are again Boltzmann-constant and temperature, N is the effective density of mobile ions and finally q is the ion-charge. [7]

2.2 Defects in crystals

In contrast to simplified and idealized crystal systems, real crystal systems contain area, line and point defects, which make diffusion in solids, as described above, possible.

Point defects

There are three types of point defects, also known as atomic crystal defects:

- impurity atoms,
- mixed crystals and
- Schottky or Frenkel defects. [8]

Without exception an ideal crystal system consists of pure substance. However, it is again different in real crystal systems. Here foreign atoms, which are smaller or bigger are embed in the crystals. These atoms are called impurity atoms. Mixed crystals are caused by the statistical distribution of components. During the formation of mixed crystals vacancies are formed. Schottky defects are ion vacancies at regular lattice sites, which are caused by migration of respective ions to the crystal's surface. Frenkel defects occur, where cations leave an initial position and migrate to an interstitial position. [8] In Figure 3 Schottky and Frenkel defects are shown.

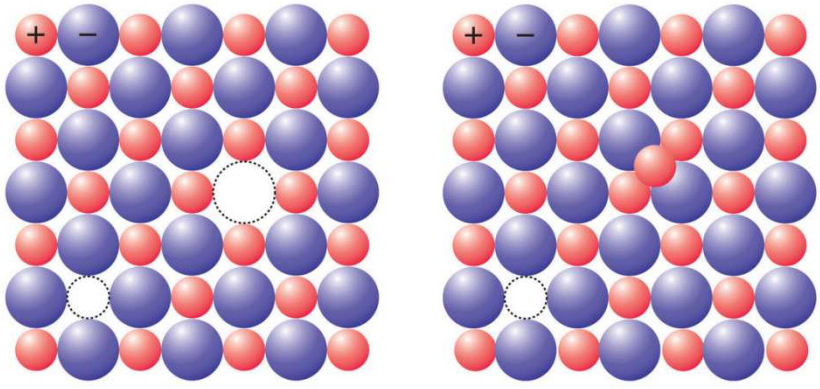

Figure 3: Presentation of Schottky and Frenkel defects. The blue spheres represent anions and the red spheres are cations. In a) the Schottky defects, with cation and anion vacancies are shown. b) presents the Frenkel defect, showing the occupied interstitial position. The figure is taken out of reference [9].

Defects in solids can be seen as advantages, because e.g. as a consequence of Schottky or Frenkel defects the crystal starts to conduct electricity, which is fundamental for solid electrolytes [8].

2.3 Basics of impedance spectroscopy

Electrochemical impedance spectroscopy (EIS) is a widespread method used in applied electrochemistry and material science. The method can be used for characterization of electrochemical behavior of systems. [10]

In this work, EIS was used to determine the conductivity of lithium argyrodites and antiperovskites.

If not stated otherwise, the following equations in this chapter are taken from reference [10].

The resistance R of a system is shown, when a current I, that is applied at a certain voltage U, flows through the system. This process is defined in Ohm's law (Equation 2.7). This equation is only valid, when voltage and current are in phase, like it is in an ideal resistor.

Ohm's law:

$$R = \frac{U}{I} \tag{2.7}$$

By noting the sample geometry, the resistance (Equation 2.8) can be defined as followed:

$$R = \rho \frac{d}{A} \tag{2.8}$$

ρ is the resistivity, d the sample-thickness and A the surface area of the sample.

The conductivity σ is the reciprocal resistivity. Thus the impedance is defined as the ratio between voltage and current and it also counts in the phase shift between entering voltage and resulting current. Therefore, when impedance is experimentally measured, an AC voltage with certain amplitude is applied within different frequencies. The voltage signal depends on time.

The mathematical context of the applied voltage $V(t)$ is shown in the next equation 2.9:

$$V(t) = V_a \sin(\omega t) \tag{2.9}$$

With V_a as the voltage amplitude, ω the angular frequency and the time t.

With different current amplitude I_a and phase φ, the resulting current output $I(t)$ is described in equation 2.10:

$$I(t) = I_a \sin(\omega t + \varphi) \tag{2.10}$$

In Figure 4, equation 2.9 and equation 2.10 are illustrated.

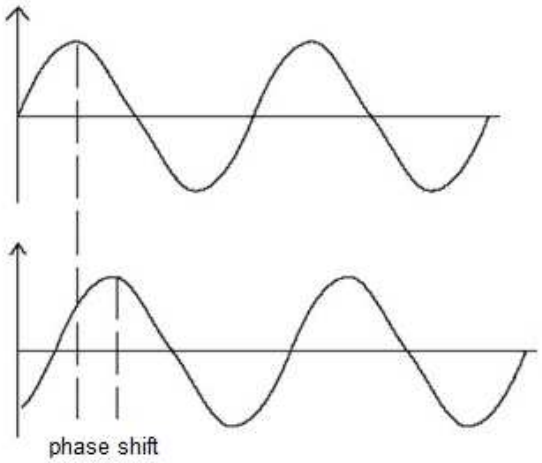

Figure 4: Illustration of the phase shift φ in EIS. The upper curve illustrates $V(t)$. The nethermost curve shows $I(t)$.

By summing up the equations above, equation 2.11 for the complex impedance Z^* can be determined:

$$Z^* = \frac{V_a \sin(\omega t)}{I_a \sin(\omega t + \varphi)} = \frac{V(t)}{I(t)} \tag{2.11}$$

Considering Euler's relation (Equation 2.12) complex impedance can be rewritten:

Euler's relation:

$$\exp(i\varphi) = \cos(\varphi) + i \sin(\varphi) \tag{2.12}$$

$$Z^* = Z' + iZ'' \tag{2.13}$$

Z' is the real part and Z'' is the imaginary part.

As seen in equation 2.13, the complex impedance is built up of two parts, the real part, which stands for the resistance to current that flows through a circuit and the imaginary part that represents the ability to store capacitive electrical energy.

The real part of conductivity σ' can be determined using equation 2.14 below:

$$\sigma' = \frac{Z'_s}{Z'^2_s + Z''^2_s} \tag{2.14}$$

This equation is used for plotting the conductivity isotherms and furthermore the Arrhenius plot.

2.4 Spectra of impedance spectroscopy

In the following two subitems the conductivity isotherms and the Nyquist plot are illustrated and described.

2.4.1 Conductivity isotherms

Conductivity spectra consist of conductivity isotherms that are obtained by plotting the real part of conductivity versus the frequency, both plotted on a double logarithm scale.

Conductivity isotherms can be divided into three regions. The first region shows the electrode polarization. Electrode polarization occurs at lower frequencies, when ions of the measured sample are blocking one of the electrodes. In the second region, the σ_{DC}-plateau, the ions achieve successful jumps between various ion sites. The third region at higher frequencies is called dispersive region. [11]

The conductivity within the σ_{DC}-plateau, which shows the long-range jumps, is independent of frequency and therefore a quasistatic region [7].

Figure 5 demonstrates a typical conductivity isotherm divided into the stated regions.

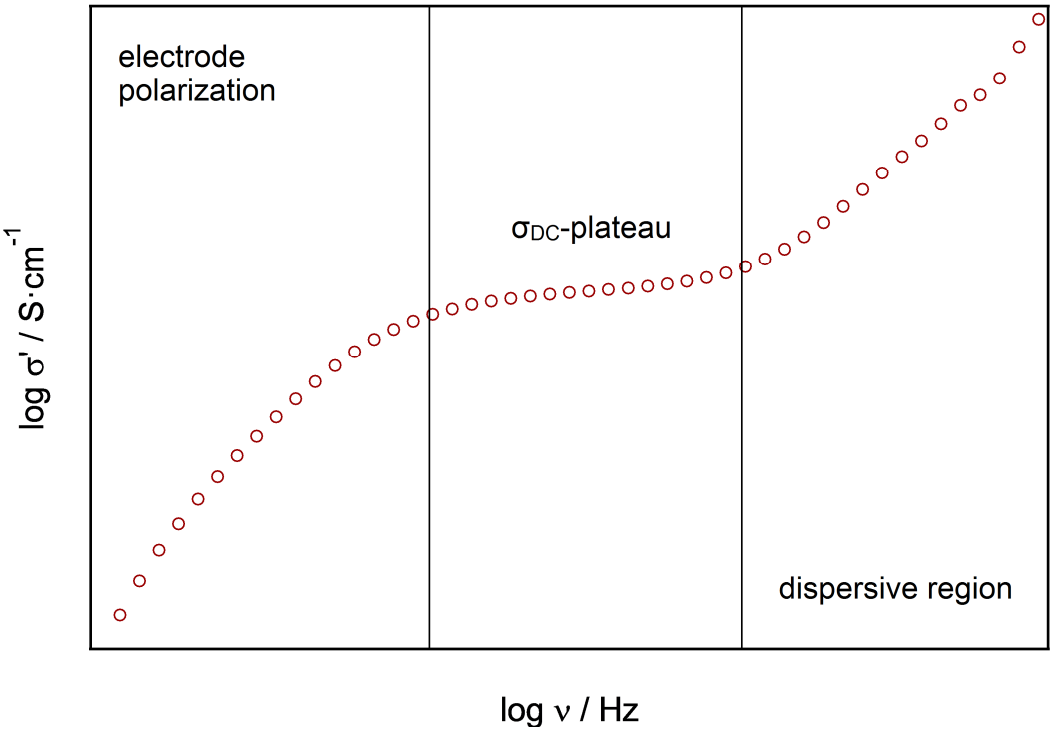

Figure 5: Schematic representation of a conductivity isotherm at a certain temperature, showing the characteristic regions.

The activation energy can be determined using the conductivity of the σ_{DC}-plateau by plotting it as log (σ_{DC}·T) against the inverse temperature (1000/T). The diagram that results is the Arrhenius plot. Via the slope of the curves the activation energy can be calculated according to the Arrhenius equation 2.15. [12]

$$\sigma_{DC} = \frac{\sigma_0}{T} \exp\left(\frac{-E_A}{k_B T}\right) \tag{2.15}$$

2.4.2 Nyquist plot

To interpret the experimental impedance data it is necessary to introduce equivalent circuit elements. Therefore it is important to take a closer look at the Nyquist plot, which represents the impedance values in a complex plane plot. The following two equations (2.16 and 2.17) are used as initial equations for calculating the overall impedance. [7]

$$Z_R = R \tag{2.16}$$

$$Z_C = \frac{1}{i\omega C} - \frac{i}{\omega C} \tag{2.17}$$

Here C represents the capacitance and R represents the resistance. In Figure 6 the corresponding Nyquist plot is illustrated.

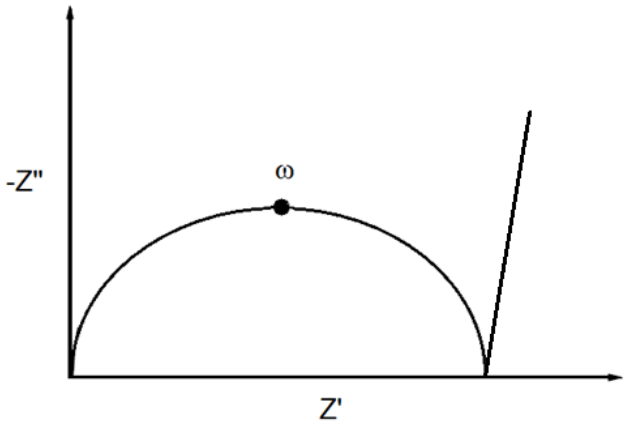

Figure 6: Nyquist plot for the impedance (-Z'' vs. Z') of a series connection.ω represents the frequency.

2.5 X-ray powder diffraction

X-ray powder diffraction is a non-destructive method for revealing crystal structure and phase compositions of prepared samples and also to gain material properties like stress and strain or grain size [13]. For the present work on sulfide ionic conductors, X-ray powder diffraction was used to verify the sample preparation and to characterize the lithium-argyrodites and the lithium-antiperovskites.

During the XRD measurement monochromatic X-rays are generated and hit the sample. Then the X-rays get diffracted in a certain angle (Bragg angle). The monochromatic X-rays occur in sealed X-ray tubes, where electrons are emitted by the cathode. Towards the anode electrons are accelerated due to a voltage difference between the electrodes. When the electrons hit the anode, X-rays are generated and get passed through an X-ray monochromator. The X-rays defeat the sample and are diffracted before they hit a detector. Destructive interferences lead to non-detectable reflections, while constructive interferences are given, if Bragg's law (Equation 2.18) is valid. [14, 15]

The relation of the distance between the planes d and the indices angle θ is described in Bragg's law

$$n\,\lambda = 2\,d\sin\theta \tag{2.18}$$

with n ϵ ℕ and λ as wavelength.

The schematic drawing of the Bragg's law is presented in Figure 7 below.

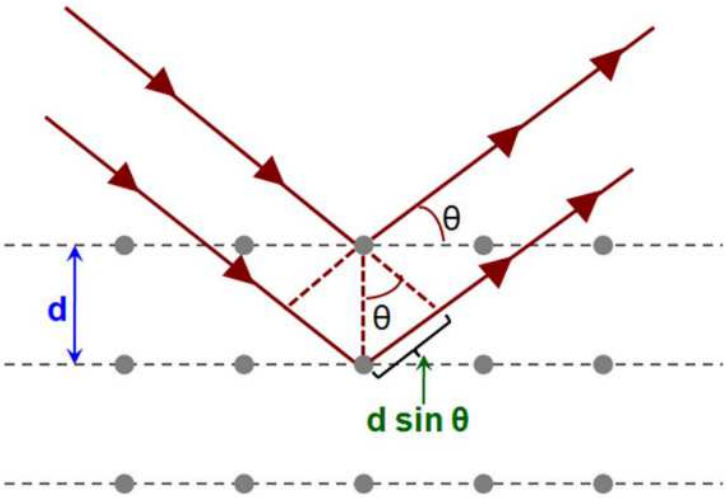

Figure 7: Schematic drawing of Bragg`s law according to reference [13].

The result of a XRD-measurement is described in a plot, where the intensity is plotted against 2 θ. The position of the reflection, but also the intensity is important. With the help of several databases, e.g. ICSD - Inorganic Crystal Structure Database, it is possible to compare positions and intensities of the reflexes and identify the compound. [14, 15]

2.6 Structure details

This chapter focuses on the structural details of the prepared sulfide ionic conductors, the lithium argyrodites and antiperovskites.

2.6.1 Lithium argyrodite

Argyrodites are compounds with the general formula A_{12-m-x}^{+} (M^{m+} Y_4^{2-}) Y_{2-x}^{2-} X_x^{-}. Here A^{+}=Li^{+}, Cu^{+}, Ag^{+}; M^{m+}=Si^{4+}, Ge^{4+}, Sn^{4+}, P^{5+}, As^{5+}; Y^{2-}=O^{2-}, S^{2-}, Se^{2-}, Te^{2-}; X^{-}=Cl^{-}, Br^{-}, I^{-} and 0≤x≤2 [16].

A high lithium ion conductivity is reported in lithium argyrodites with the general formula Li_6PS_5X, where X=Cl, Br, I and 0≤x≤1. Moreover sulfur-based lithium argyrodites are cheaper than argyrodites based on selenium. These two properties make them to promising candidates for solid electrolytes in solid state lithium ion batteries. [17]

The majority of argyrodites shows a cation-disordered aristotype-structure[2] in a $F\bar{4}3m$ space group with icosahedral cages. Some argyrodites are crystallized in lower symmetry space group $P2_13$ in an intermediate state of disorder and some are in cation-ordered

[2] *An aristotype-structure is a high-symmetry structure type. It can be viewed as an idealized version of a lower-symmetry structure.*

orthorhombic space groups *Pmn*2_1 and *Pna*2_1. Other argyrodite structures crystallize in the monoclinic space group *Cc*. For argyrodites, which are rich in halides, the structure type is the orthorhombic structure in space group *Pnma* (see Figure 8a) with $Ag_6(GeS_4)X_2$, where X=Cl, Br and $Ag_6(SnS_4)Br_2$, which are members of "non-metallic filled $NaHg_2$ phases" family. The non-metal atoms sulfur and the halogens build up a structure that corresponds to the mentioned $NaHg_2$, which is X_2S_4 with germanium in tetrahedral holes and silver in tetrahedral and octahedral holes (see Figure 8b). [16]

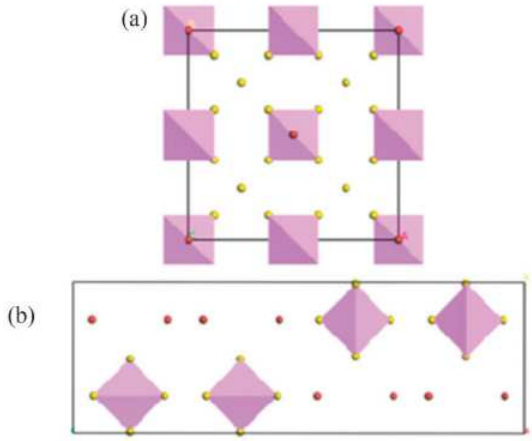

Figure 8: (a) Argyrodite structure and (b) $NaHg_2$-structure, both according to reference [16]*. The red spheres represent the X^- anions, while mobile ions are left out. The purple tetrahedrons illustrate the MS_4^{8-}-groups.*

In contrast to lithium metal, halogens like chlorine, bromine and iodine are highly electronegative. Thus halogens are quite stable once they accept an additional electron to form an anion. Lithium likely donates an electron and the type of bonding for LiX (X: Cl, Br, I) is called ionic bonding. [18]

During the work on this master's thesis the following lithium argyrodites were synthesized and characterized:

Table 1: Prepared lithium argyrodite samples

Lithium argyrodites	
LPSB	Li_6PS_5Br
LPSBI 75/25	$Li_6PS_5Br_{0.75}I_{0.25}$
LPSBI 25/75	$Li_6PS_5Br_{0.25}I_{0.75}$
LPSI	Li_6PS_5I
LPSCB 75/25	$Li_6PS_5Cl_{0.75}Br_{0.25}$
LPSCB 25/75	$Li_6PS_5Cl_{0.25}Br_{0.75}$
LPSC	Li_6PS_5Cl

2.6.2 Fluorine - doped lithium argyrodite

Doping is one of the most commonly used methods for optimizing or changing material properties in electrochemistry. Therefore an element or compound is doped into the substrate in small addition. [19]

Lithium Fluoride is researched on as a doping material due to its chemical properties and similar crystal structure in this thesis.

Table 2: Prepared fluorine - doped lithium argyrodite samples.

Fluorine-doped lithium argyrodites	
LPSCF 95/05	$Li_6PS_5Cl_{0.95}F_{0.05}$
LPSBF 95/05	$Li_6PS_5Br_{0.95}F_{0.05}$
LPSIF 95/05	$Li_6PS_5I_{0.95}F_{0.05}$
LPSIF 85/15	$Li_6PS_5I_{0.85}F_{0.15}$
LPSIF 50/50	$Li_6PS_5I_{0.50}F_{0.50}$

2.6.3 Antiperovskite

Inorganic compounds with a cubic perovskite structure as shown in Figure 9, where the cations are replaced by anions and the anions are replaced by cations are called antiperovskites or inverse perovskites. The general formula is A_3BX. A and B are cations, while X stands for the anion. [20]

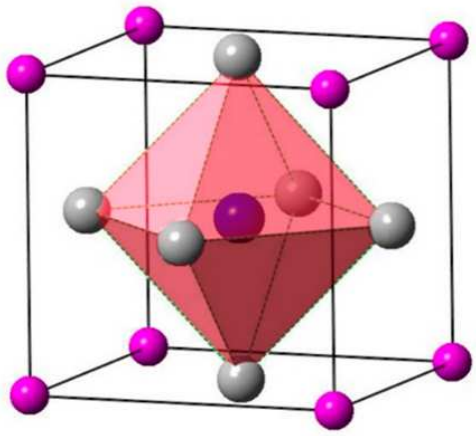

Figure 9: Structural representation of a general cubic antiperovskite structure A_3BX according to reference [21]*. The grey spheres are A. B are the pink spheres and the blue sphere in the middle of the unit cell is the halogen X.*

In context of this master's thesis lithium-antiperovskites with the structure Ag_3SI and Li_3SI were prepared.

3 Experimental part

In the experimental part the solid-state synthesis route as well as the sample preparation details for X-ray powder diffraction and impedance spectroscopy is shown.

3.1 Lithium argyrodites

The lithium argyrodite-type structures Li_6PS_5X (X: stoichiometric mixtures of Cl, Br, I, and F) were prepared using mechanical milling followed by annealing.

3.1.1 Sample preparation

The whole experimental process was done under dry argon atmosphere to exclude contamination with oxygen and moisture.

Therefore Li_2S, P_2S_5, LiX (X: Cl, Br, I and F) were mixed in stoichiometric proportions and milled in a ball mill according to reaction equation 3.1.

$$5\ Li_2S + P_2S_5 + 2\ LiX \rightarrow 2\ Li_6PS_5X \qquad (3.1)$$

The grinding beakers were filled with a total mass of 5 g of the reactants and 180 milling balls (in a diameter of 5 mm) made up of ZrO_2. The exact composition of the reactants is summarized in the appendix A. A total milling time of 4 hours (5 min milling and 15 min pause) and a rotation speed of 400 rpm was set. For further handling pellets with a diameter of 5 mm were pressed and filled into quartz ampoules, which were heated before at 300 °C to avoid again contamination with moisture. Afterwards the obtained pellets were annealed for seven days at 550 °C with a heating rate of 5 min/°C.

The temperature program of the annealing process is shown in Figure 10.

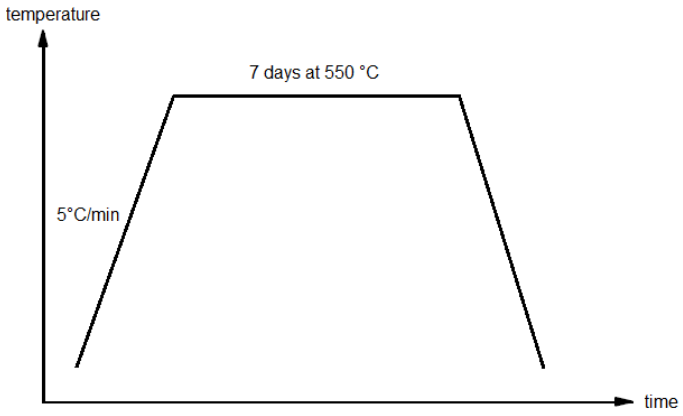

Figure 10: Temperature program of the annealing process of lithium argyrodites.

3.1.2 X-ray powder diffraction

The structural characterization of the Argyrodites was performed by X-ray powder diffraction (XRPD). For the measurement the pellets were ground. The received powders were measured at a Bruker D8 Advance diffractometer with Bragg Brentano geometry using CuKα radiation. The measurement was done in a 2Θ-range from 20° to 100° with a step size of 0.02° for 2 seconds. The spectrograms were carried out at room temperature. A mercapto foil was used to keep the sample away from air.

3.1.3 Impedance spectroscopy

For the impedance measurements electrodes with a thickness of 100 nm were applied at each side of the pellets by gold evaporation at 45 mA with a LEICA EM SCD 050 evaporator. The electrochemical impedance spectroscopy was measured with a Novocontrol Concept 80 broadband dielectric spectrometer using a frequency range from 10 mHz to 10 MHz and a temperature range from 173.15 K to 453.15 K in steps of 20 K, which was controlled by a QUATRO cryosystem.

3.2 Antiperovskites

The antiperovskites Ag_3SI and Li_3SI were also prepared using mechanical milling followed by annealing.

3.2.1 Sample preparation

A dry argon atmosphere was used as working atmosphere to exclude contamination with oxygen or moisture. The educts were mixed in stoichiometric proportions and milled in a high energy ball mill according to the following reaction equations (equation 3.2 and 3.3).

$$Ag_2S+AgI \rightarrow Ag_3SI \quad (3.2)$$

$$Li_2S+LiI \rightarrow Li_3SI \quad (3.3)$$

The grinding beakers were filled with a total mass of 5 g of educts. 180 milling balls with a diameter of 5 mm made up of ZrO_2 were added. The exact compositions of the reactants are summarized in the appendix A.

For the first samples a total milling time of 4 hours and a rotation speed of 400 rpm was set. Further samples were milled for 10 hours and 600 rpm. For further handling pellets (diameter: 5 mm) were pressed. Afterwards a part of the obtained pellets was annealed for five days at 550 °C and two further days at 220 °C. In Figure 11 the temperature program of the annealing process is shown.

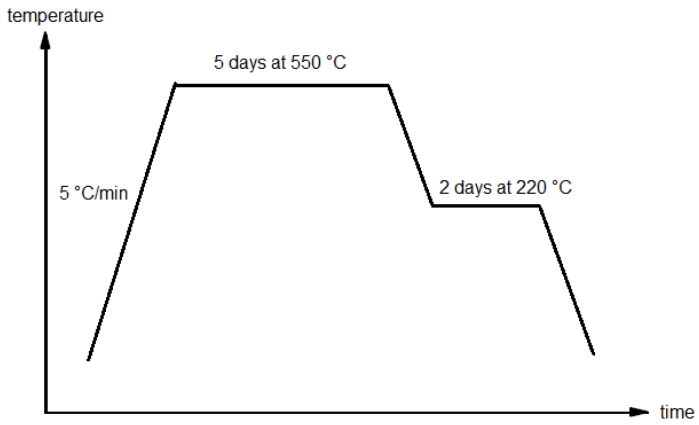

Figure 11: Temperature program of the annealing process of antiperovskites.

3.2.2 X-ray powder diffraction and impedance spectroscopy

The measurements were carried out under the same conditions and with the same equipment as mentioned before on the argyrodites (chapters 3.1.2 and 3.1.3).

4 Results and discussion

In order to determine structural details and electrochemical properties of lithium argyrodites, lithium argyrodites doped with fluorine and antiperovskites Ag_3SI and Li_3SI the results of X-ray powder diffraction and impedance spectroscopy are calculated and furthermore interpreted and compared among each other.

4.1 Lithium argyrodite

The sample characterization via X-ray powder diffraction and impedance spectroscopy of the prepared lithium argyrodites are described below.

4.1.1 Sample characterization via X-ray powder diffraction

The lithium argyrodite ionic conductors Li_6PS_5X were synthesized with various ratios of the halogen X according to Table 3.

Table 3: Prepared samples of lithium argyrodites with different ratios of halogens.

Lithium argyrodites	
LPSBI 75/25	$Li_6PS_5Br_{0.75}I_{0.25}$
LPSBI 25/75	$Li_6PS_5Br_{0.25}I_{0.75}$
LPSCB 75/25	$Li_6PS_5Cl_{0.75}Br_{0.25}$
LPSCB 25/75	$Li_6PS_5Cl_{0.25}Br_{0.75}$

As the table above illustrates, chlorine and iodine were not mixed up together. The ionic radii of these two elements are too different. According to Shannon the ionic radius of iodine is 2.20 Å and chlorine has an ionic radius of 1.81 Å. [22] Therefore two different cubic phases instead of one cubic phase would occur. In Figure 12 the XRPD pattern of all samples are shown including the reference pattern of ICSD.

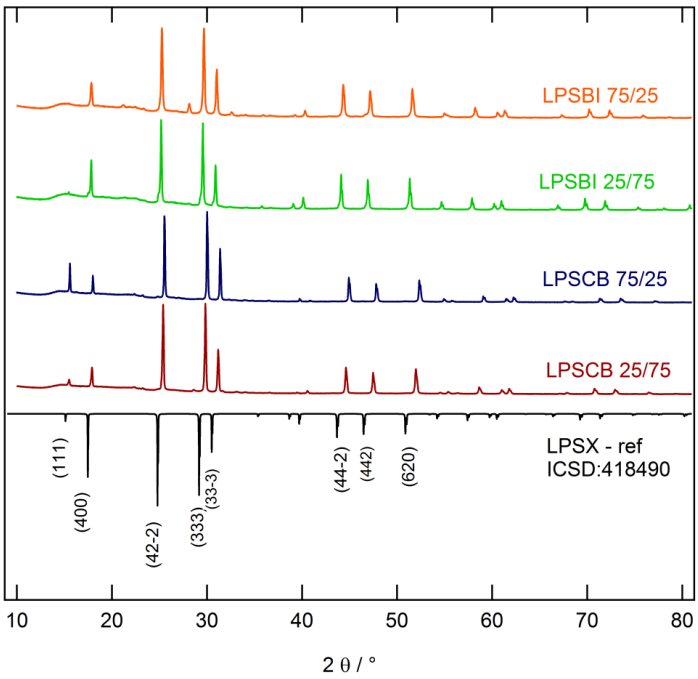

Figure 12: Measured X-ray powder diffraction pattern of the prepared samples Li_6PS_5X with X: $Br_{0.75}I_{0.25}$, $Br_{0.25}I_{0.75}$, $Cl_{0.75}Br_{0.25}$ and $Cl_{0.25}Br_{0.75}$.

As Figure 12 illustrates, the phases are pure. There are only impurities below 0.8 wt%, which can be neglected as they are likely to come from the sample carrier. The hump at lower angles comes from the mercapto foil, which was used for isolating the samples to avoid contamination with moisture.

With the help of X-ray powder diffraction, the lattice parameters could be determined as well. In Figure 13 the lattice parameters of the lithium argyrodites are exemplified.

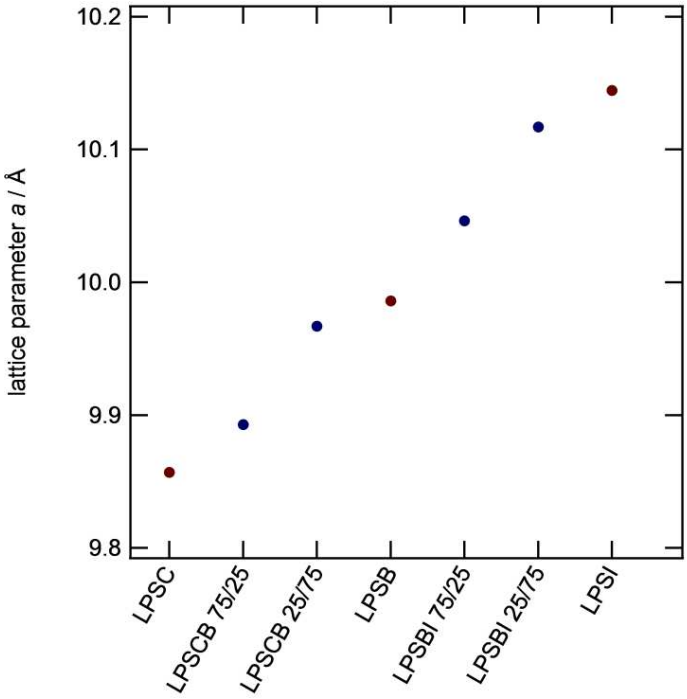

Figure 13: Lattice parameter obtained from X-ray powder diffraction of the prepared samples Li_6PS_5X with X: Cl, Br, I, $Br_{0.75}I_{0.25}$, $Br_{0.25}I_{0.75}$, $Cl_{0.75}Br_{0.25}$ and $Cl_{0.25}Br_{0.75}$. Sample Li_6PS_5Cl has the smallest and sample Li_6PS_5I the largest lattice parameter.

Table 4 lists the calculated lattice parameters.

Table 4: Calculated lattice parameter a / Å of lithium argyrodites.

Sample	Lattice parameter / Å	Volume / Å^3
Li_6PS_5Cl	9.85(7)	957.7
$Li_6PS_5Cl_{0.75}Br_{0.25}$	9.89(3)	968.2
$Li_6PS_5Cl_{0.25}Br_{0.75}$	9.96(7)	990.1
Li_6PS_5Br	9.98(6)	995.8
$Li_6PS_5Br_{0.75}I_{0.25}$	10.04(6)	1013.9
$Li_6PS_5Br_{0.25}I_{0.75}$	10.11(7)	1035.5
Li_6PS_5I	10.14(5)	1044.1

Table 5: Ionic radii according to Shannon [22].

Element	Coordination	Ionic radius / Å
Cl	6	1.81
Br	6	1.96
I	6	2.20

As stated in the Table 5 chlorine has a smaller ionic radius than bromine and bromine has a smaller ionic radius than iodine. The sample Li_6PS_5Cl has the smallest ionic radius with 9.86 Å and Li_6PS_5I has the biggest radius with 10.15 Å (see Table 4). Hence the expansion of the unit cell is expected due to increased ionic radii of chlorine, bromine and iodine.

The lithium argyrodite samples follow the argyrodite structure of $F\bar{4}3m$ symmetry as shown in Figure 14. Consequently the solid state reaction of the argyrodite samples was successful.

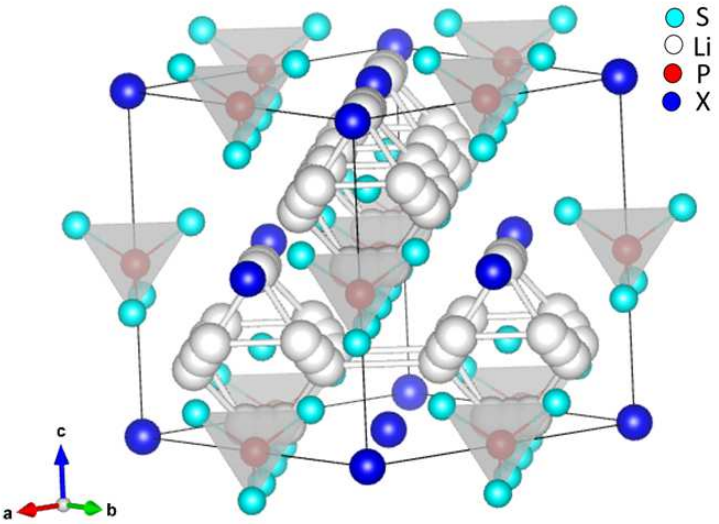

Figure 14: General crystal structure of the lithium – argyrodite.

In the ordered structure, as shown in Figure 14, X^- anions form a cubic close-packed lattice with PS_4^{3-} tetrahedra in the octahedral sites and the free S^{2-} in half of the tetrahedral holes. The free S^{2-}anions and the corner of the PS_4^{3-} tetrahedra form polyhedra, which enclose two different lithium positions. As shown in Figure 15, the lithium-positions form localized cages in which multiple jump-processes are possible. Jumps between the lithium positions, the so called intracage jumps, as well as intercage jumps and doublet jumps can occur. The intercage jumps are suggested to dominate long-range transport, and site disorder is known to affect the conductivity. [23]

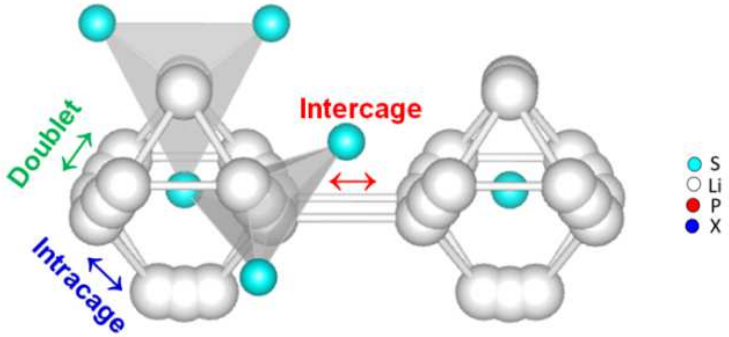

Figure 15: Different two lithium positions, in which three different jumps can occur: intercage, intracage and doublet jumps.

Higher site disorders according to the prepared bromine and chlorine argyrodites influence the jump rate. In comparison to that, the lithium argyrodites with iodine show a lower site disorder, because of larger ionic radius.

In 2008 Deiseroth reported that the intercage jump in Li_6PS_5I is hindered, which could also be a possible reason for that [24].

4.1.2 Sample characterization via impedance spectroscopy

To find out more about the lithium-diffusion in the lattice of the prepared samples with various halides and different halide contents an electrochemical impedance spectroscopy at different temperatures and different frequencies was carried out. The real part of conductivity σ' was plotted against the frequency v on a double logarithm scale. As an example the conductivity isotherms of $Li_6PS_5Br_{0.75}I_{0.25}$ are illustrated in Figure 16. According to the Arrhenius process the temperature-dependence of the conductivity can be described.

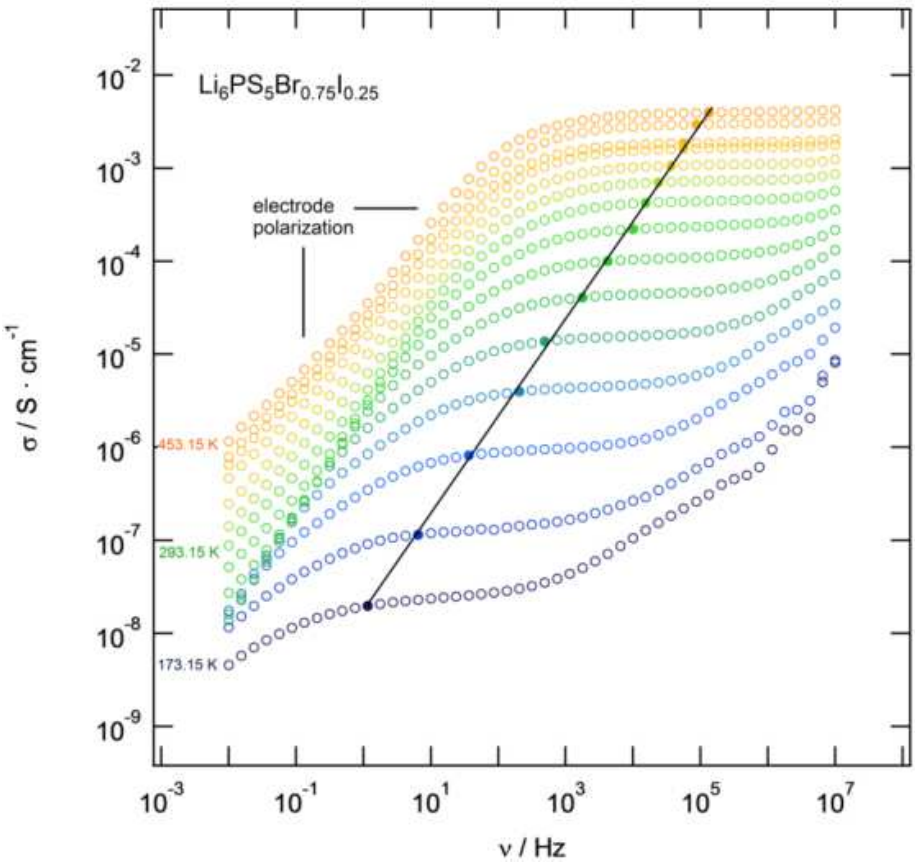

Figure 16: Conductivity isotherms of $Li_6PS_5Br_{0.75}I_{0.25}$ at a frequency range from 10 mHz to 10 MHz and a temperature range from 173.15 K to 453.15 K. At lower frequencies the isotherms show electrode polarization. At higher frequencies the σ_{DC}-plateau is visible

At lower frequencies the isotherms show dielectric phenomena like electrode polarization, whereas at higher frequencies the σ_{DC}-plateau is visible. It reflects the long-range ion transport.

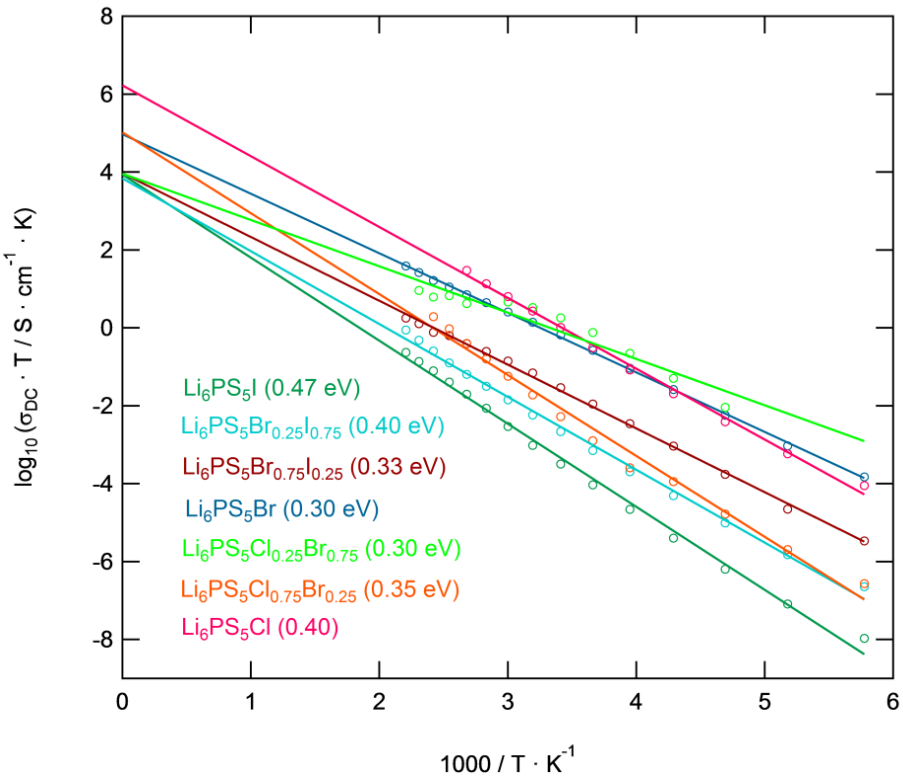

Figure 17: The Arrhenius plot shows the change of σ of the lithium argyrodite samples as a function of inverse temperature.

For $Li_6PS_5Br_{0.75}I_{0.25}$ the distinct direct current reaches an activation energy of 0.333 eV (see Figure 17).

In Table 6 the calculated activation energies and conductivities at room temperature of the lithium argyrodites are summarized.

Table 6: Calculated activation energy E_A / eV and conductivities σ_{RT} / S·cm^{-1} of lithium argyrodites.

Sample	E_A / eV	σ_{RT} / S·cm^{-1}
Li_6PS_5Cl	0.39(6)	$3.47 \cdot 10^{-3}$
$Li_6PS_5Cl_{0.75}Br_{0.25}$	0.35(0)	$1.20 \cdot 10^{-3}$
$Li_6PS_5Cl_{0.25}Br_{0.75}$	0.30(4)	$6.06 \cdot 10^{-3}$
Li_6PS_5Br	0.29(6)	$2.27 \cdot 10^{-3}$
$Li_6PS_5Br_{0.75}I_{0.25}$	0.33(3)	$1.06 \cdot 10^{-4}$
$Li_6PS_5Br_{0.25}I_{0.75}$	0.39(7)	$7.40 \cdot 10^{-6}$
Li_6PS_5I	0.47(0)	$1.09 \cdot 10^{-6}$

Li_6PS_5Cl shows the lowest and Li_6PS_5I the highest activation energy. The difference in Li^+-conductivity between Li_6PS_5I and Li_6PS_5Cl, which is several orders of magnitude, is caused by the distribution of the halogen ions across the available crystallographic centers. This suggests that changing the halogen distribution in lithium argyrodites can

increase the Li^+-conductivity of these materials. The high ionic conductivity of the lithium argyrodite Li_6PS_5Cl is characterized by localized ion-jumps and lattice vibrations. The low ionic conductivity of the samples with a high amount of iodine (Li_6PS_5I and $Li_6PS_5Br_{0.25}I_{0.75}$) is ascribable to the high ionic radius of the iodide ion due to the fact, that iodide is a large negatively charged ion and therefore highly polarizable.

In Figure 18 the relationship of the pre-factor and activation energy is illustrated.

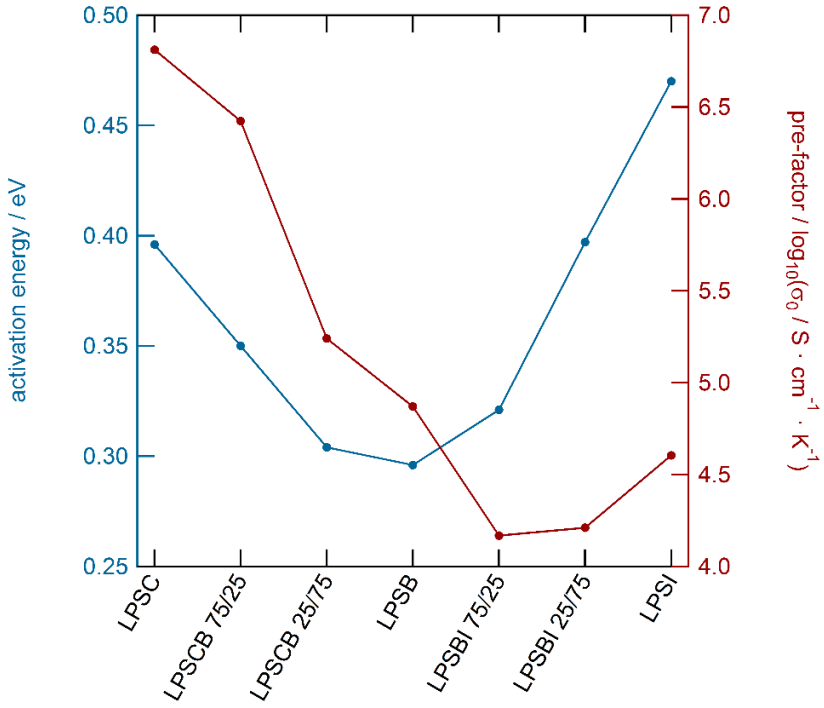

Figure 18: The blue line shows the activation energy depending on the halogen content of the lithium argyrodites. The red line shows the pre-factor vs. the halogen content of Li_6PS_5X.

With an increasing ionic radius and decreasing lattice stiffness the activation energy and pre-factor are decreasing. The substitution of heavier halide anions leads to decreasing in activation barrier and σ_0 as it is expected in the Meyer-Nedel rule. [25] The samples with iodine do not follow this rule due to absence of the site disorder. In Table 7 the calculated pre-factors are summarized.

Table 7: Calculated pre-factors of lithium argyrodite samples.

Sample	Pre-factor
Li_6PS_5Cl	6.812
$Li_6PS_5Cl_{0.75}Br_{0.25}$	6.424
$Li_6PS_5Cl_{0.25}Br_{0.75}$	5.240
Li_6PS_5Br	4.870
$Li_6PS_5Br_{0.75}I_{0.25}$	4.168
$Li_6PS_5Br_{0.25}I_{0.75}$	4.210
Li_6PS_5I	4.604

In Figure 16 the isotherms show a σ_{DC}-plateau with an activation energy of 0.333 eV according to sample $Li_6PS_5Br_{0.75}I_{0.25}$. To point up that there is one plateau, the permittivity plot (Figure 20) as well as the Nyquist plot (Figure 19) were used for calculating the capacities. Therefore the equation for a parallel-plate capacitor was used, which is shown in equation 4.1.

$$C = \varepsilon_0 \cdot \varepsilon_r \cdot \frac{A}{d} \tag{4.1}$$

ε_0 constitutes the electric field constant[3], which is $8.854 \cdot 10^{-12}$ F·m^{-1}. A represents the sample's area and d the thickness of the pellet. ε_r is the relative permittivity. The calculated capacity is 7.93 pF. The value does match the capacity that can be calculated with the help of the Nyquist plot (see Figure 19), which is also in the Picofarad-range. This value indicates a bulk process. [26]

The capacity of the sample $Li_6PS_5Br_{0.75}I_{0.25}$ in the Nyquist plot can be calculated through ϖ_{el} as followed.

$$\varpi_{el} = \frac{1}{RC} \tag{4.2}$$

Here ϖ_{el} represents the relaxation frequency and R stands for the resistance.

[3] https://physics.info/constants/

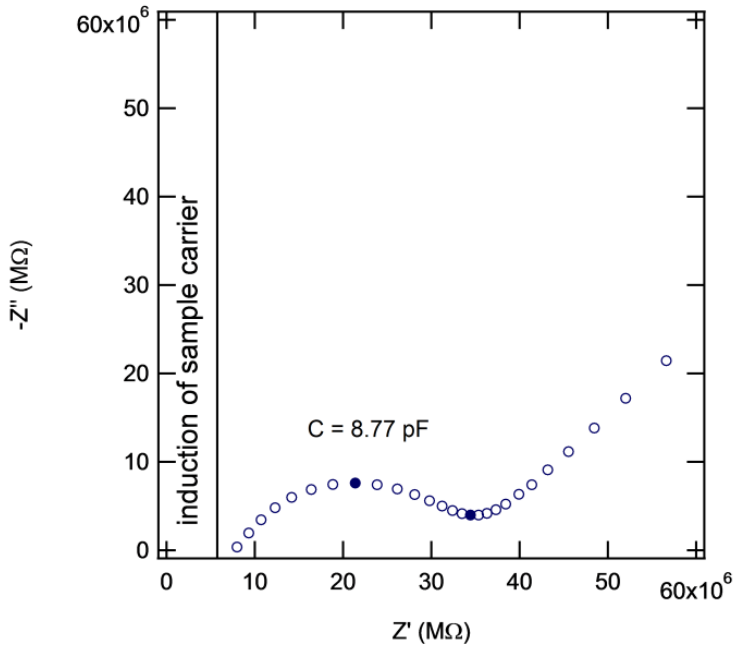

Figure 19: Nyquist plot of the real part vs. the negative imaginary part of sample $Li_6PS_5Br_{0.75}I_{0.25}$ at 333.15 K. A depressed semicircle can be seen that corresponds to bulk. The region on the left shows the induction of the sample carrier.

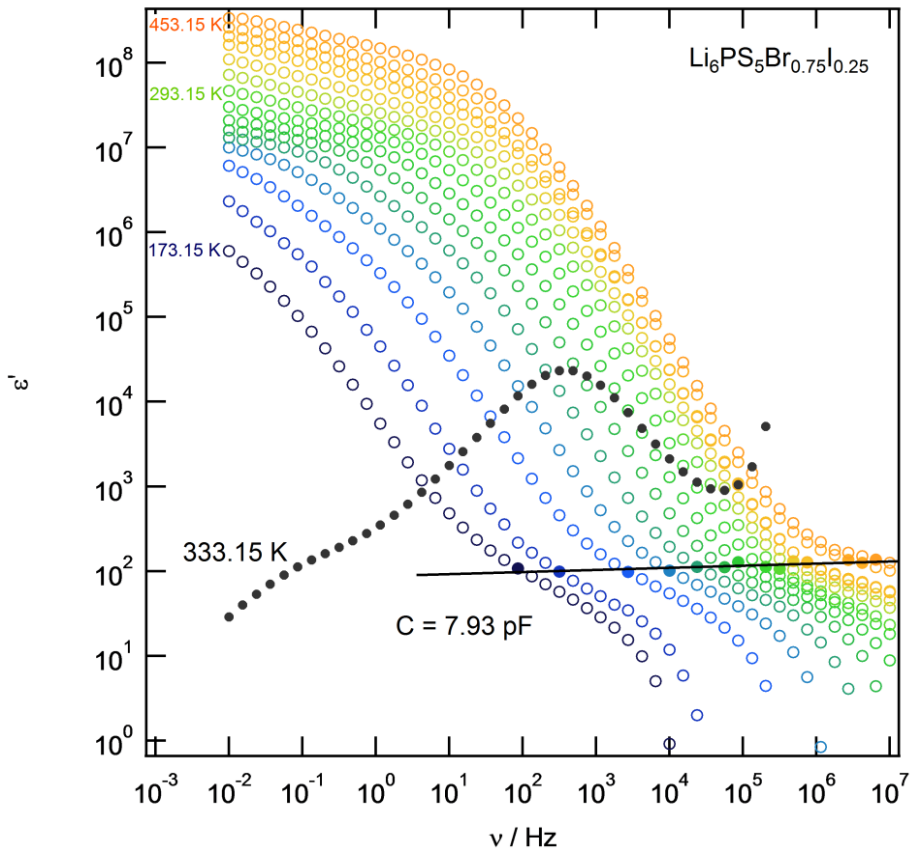

Figure 20: Here the real part of permittivity and the loss factor tan δ as a function of frequency of the sample $Li_6PS_5Br_{0.75}I_{0.25}$ are shown. The black dots represent the loss factor at 333.15 K that approves the plateau. The black line shows the plateau, which corresponds to the capacity for bulk (Picofarad-range).

The sample Li_6PS_5Cl is the only lithium argyrodite sample that shows two σ_{DC}-plateaus and therefore a bulk- and grain boundary-contribution. According to its permittivity plot capacities of C_{bulk}=4.14 pF and $C_{g.b.}$=1.16 nF were obtained using equation 4.1. The Nyquist plot underlines the results. It shows two semicircles and the estimated capacities suit each other. For C_{bulk}=4.36 pF and $C_{g.b.}$=2.69 nF were calculated again via equation 4.2.

4.2 Lithium argyrodites doped with fluorine

The following chapters describe the sample characterization via X-ray powder diffraction and impedance spectroscopy of the prepared lithium argyrodites doped with fluorine.

4.2.1 Sample characterization via X-ray powder diffraction

Figure 21 and Figure 22 show the X-ray diffraction pattern of the fluorine-doped lithium argyrodites and the corresponding reference material, extracted of the ICSD database. Most reflections match quite good with those of the reference.

Some reflections at lower diffraction angles are only weak identifiable in the samples $Li_6PS_5Br_{0.95}F_{0.05}$ and $Li_6PS_5I_{0.95}F_{0.05}$ compared to the reference which is due to the background, coming from amorphous parts of the samples.

The sample $Li_6PS_5Cl_{0.95}F_{0.05}$ does not match with the reference pattern. Therefore the solid state reaction does not work, which can be improved through longer annealing times or another heating rate.

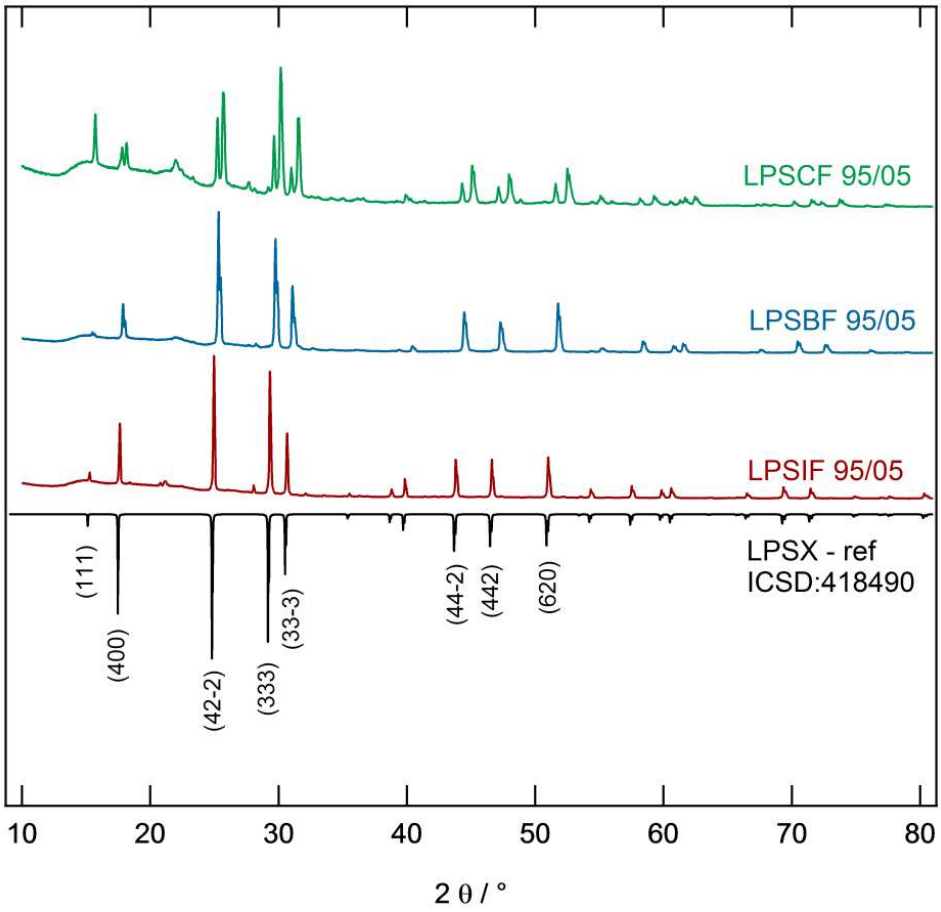

Figure 21: X-ray powder diffraction patterns of the samples $Li_6PS_5X_{0.95}F_{0.05}$ with X=Cl, Br and I.

Therefore it was dedicated to take a closer look on the argyrodite samples with iodine and fluorine. In Figure 21 three different compositions of the lithium argyrodites with iodine and fluorine are shown. It is obvious that the sample $Li_6PS_5I_{0.50}F_{0.50}$ is not phase pure. Two different cubic phases occurred. The samples $Li_6PS_5I_{0.95}F_{0.05}$ and $Li_6PS_5I_{0.85}F_{0.15}$ are phase pure. The reflexes correspond well with the reference according to ICSD database, which is indicated by the black pattern. The small reflexes at ~ 20° and ~ 29° can be assigned to LiF and LiI.

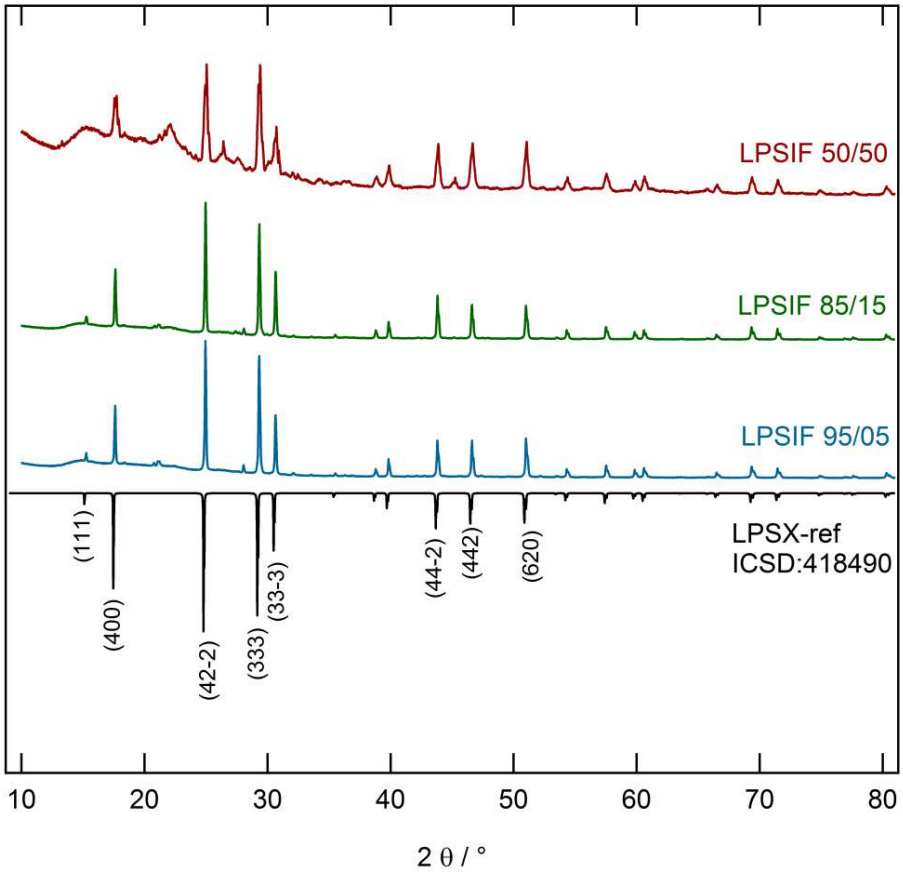

Figure 22: X-ray powder diffraction patterns of the samples $Li_6PS_5I_{0.95}F_{0.05}$, $Li_6PS_5I_{0.85}F_{0.15}$ and $Li_6PS_5I_{0.50}F_{0.50}$.

The reflexes are also identical with the ones of lithium argyrodites without fluorine content. But there is a only slight difference in the lattice parameters.

Table 8 assumes the lattice parameters *a* / Å of the samples $Li_6PS_5I_{0.95}F_{0.05}$, $Li_6PS_5I_{0.85}F_{0.15}$ and $Li_6PS_5I_{0.50}F_{0.50}$.

Table 8: Calculated lattice parameter a [Å] of fluorine-doped lithium argyrodites with iodine and fluorine.

Sample	Lattice parameter / Å
Li_6PS_5I	10.14(5)
$Li_6PS_5I_{0.95}F_{0.05}$	10.14(9)
$Li_6PS_5I_{0.85}F_{0.15}$	10.15(6)
$Li_6PS_5I_{0.50}F_{0.50}$	10.20(6) and 10.15(9)

With increasing fluorine content the lattice parameter increases to a small extent.

4.2.2 Sample characterization via impedance spectroscopy

Figure 23 and Figure 24 show the conductivity isotherms as well as the Arrhenius plot of the lithium argyrodite sample with a halogen amount of 95 % iodine and 5 % fluorine.

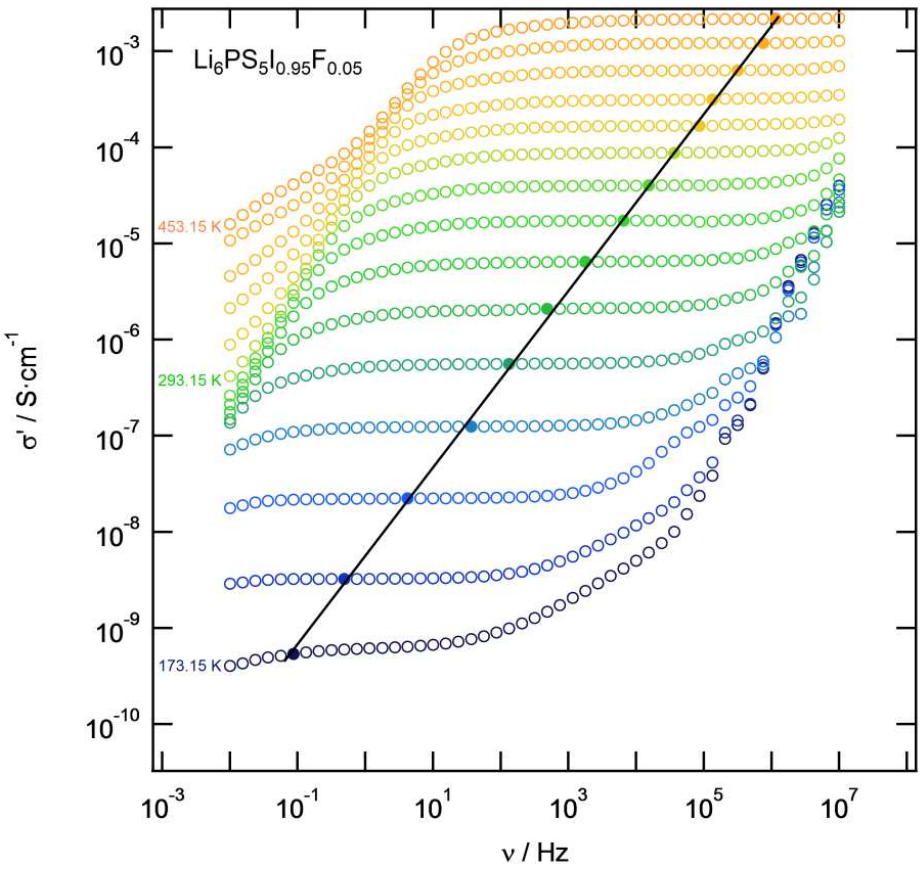

Figure 23: Conductivity isotherms of $Li_6PS_5I_{0.95}F_{0.}05$ at a frequency range from 10 mHz to 10 MHz and a temperature range from 173.15 K to 453.15 K.

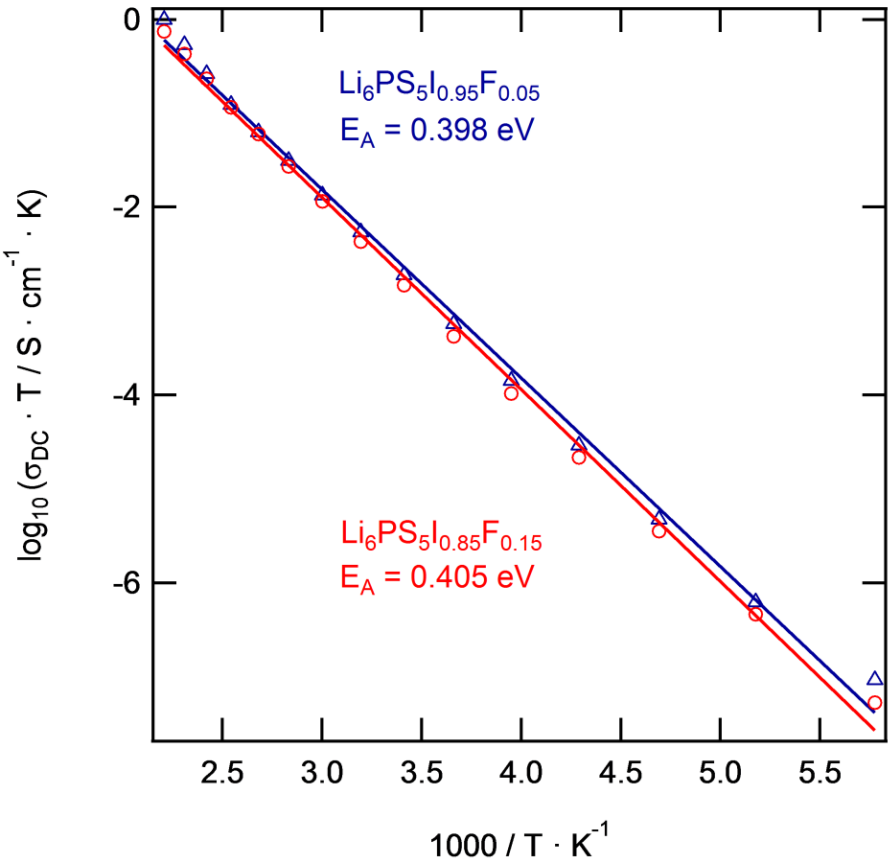

Figure 24: The Arrhenius plot shows the change of σ of the samples $Li_6PS_5I_{0.95}F_{0.05}$ and $Li_6PS_5I_{0.85}F_{0.15}$ as a function of inverse temperature.

The obtained conductivity of $Li_6PS_5I_{0.95}F_{0.05}$ at room temperature is $6.5 \cdot 10^{-6}$ S·cm^{-1}. When the fluorine content is increased, no change in conductivity can be detected. The conductivities at room temperature as well as the activation energies, which are also nearly the same, are assumed in Table 9.

Table 9: Calculated activation energy E_A / eV and conductivities σ_{RT} / S·cm^{-1} of lithium argyrodites doped with fluorine.

Sample	E_A / eV	σ_{RT} / S·cm^{-1}
Li_6PS_5I	0.47(0)	$1.09 \cdot 10^{-6}$
$Li_6PS_5I_{0.95}F_{0.05}$	0.39(8)	$6.458 \cdot 10^{-6}$
$Li_6PS_5I_{0.85}F_{0.15}$	0.40(5)	$5.163 \cdot 10^{-6}$
$Li_6PS_5I_{0.50}F_{0.50}$	0.39(5)	$6.376 \cdot 10^{-6}$

In comparison with the non-doped lithium argyrodite sample Li_6PS_5I, where a conductivity at room temperature of $1.09 \cdot 10^{-6}$ S·cm^{-1} was reached, the fluorine-doped samples show conductivities in the same magnitude. The activation energy of Li_6PS_5I is higher with 0.47(0) eV.

The permittivity plot (Figure 25) was used for calculating the capacities. The equation for a parallel-plate capacitor was used, which is already cited in equation 4.1.

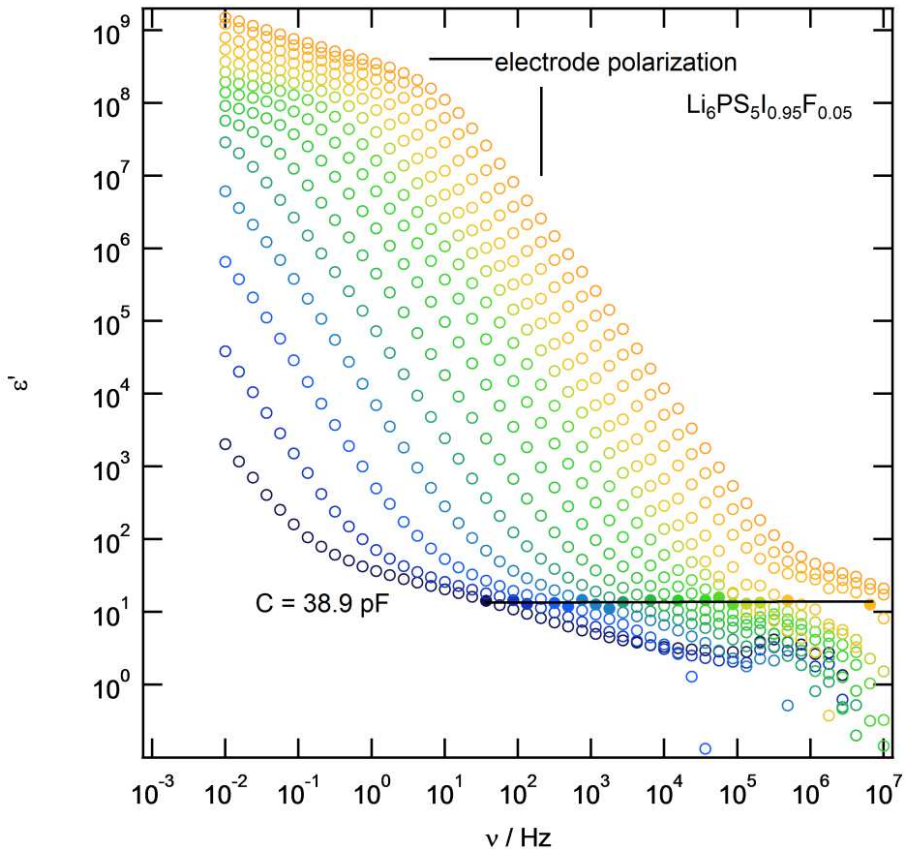

Figure 25: The real part of permittivity as a function of frequency of the sample $Li_6PS_5I_{0.95}F_{0.05}$ is shown.

In order to be able to determine the exact fluorine content and the residence probability of the fluorine anion, a Scanning Electron Microscopy (SEM) would have to be carried out.

4.3 Antiperovskite Ag_3SI

The sample characterization via X-ray powder diffraction and impedance spectroscopy of the prepared antiperovskite Ag_3SI are described below.

4.3.1 Sample characterization via X-ray powder diffraction

The structure of the silver antiperovskite compound Ag_3SI has been studied in order to clarify the microscopic origin of the structural phase transition.

Figure 26 shows the XRPD pattern of the antiperovskite sample Ag_3SI.

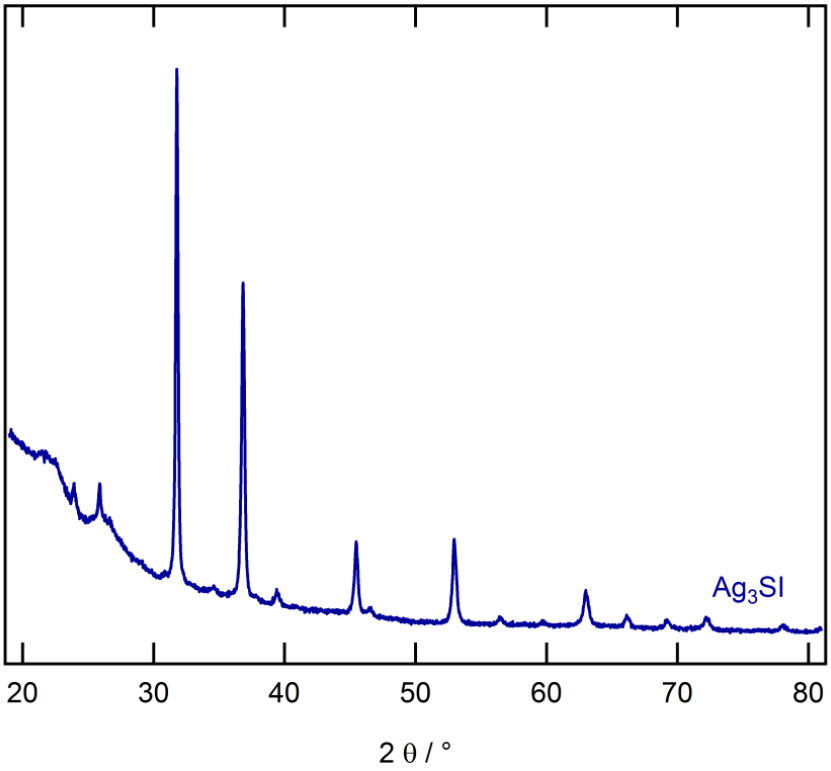

Figure 26: XRPD pattern of the antiperovskite Ag_3SI.

The hump at lower angles (2Θ=20° to 30°) comes from the mercapto foil on the sample carrier. The foil was used to isolate the sample and to avoid degradation with moisture and air.

Due to the slow cooling of the *α*-Ag_3SI (550 °C to 220 °C), the *β*-phase of Ag_3SI was stabilized. A long-range ordering of the two cation species lowers the symmetry to P*m*3*n* directions and towards the tetrahedral sites, with a single Ag^+ randomly occupying one of four free positions. [27]

Figure 27 shows the crystal structure of the antiperovskite *β*-Ag_3SI.

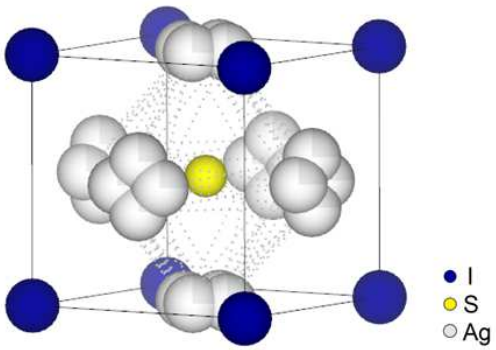

Figure 27: General crystal structure of cubic β-Ag_3SI antiperovskite.

In the *β*-phase of the silver antiperovskite Ag_3SI the body-centered cubic structure is built up of a simple cubic iodide and sulfide ions sub-lattices. In a simple cube the iodide ions

are placed in the corners of the cube. There is also a group of four vicinities. The three Ag ions are recognized to be distributed statistically over them. [28]

4.3.2 Sample characterization via impedance spectroscopy

Conductivity measurements of the silver antiperovskite sample Ag_3SI were studied by means of impedance spectroscopy. In the following, results of the annealed Ag_3SI are presented. Figure 28 shows the conductivity isotherms of the antiperovskite Ag_3SI.

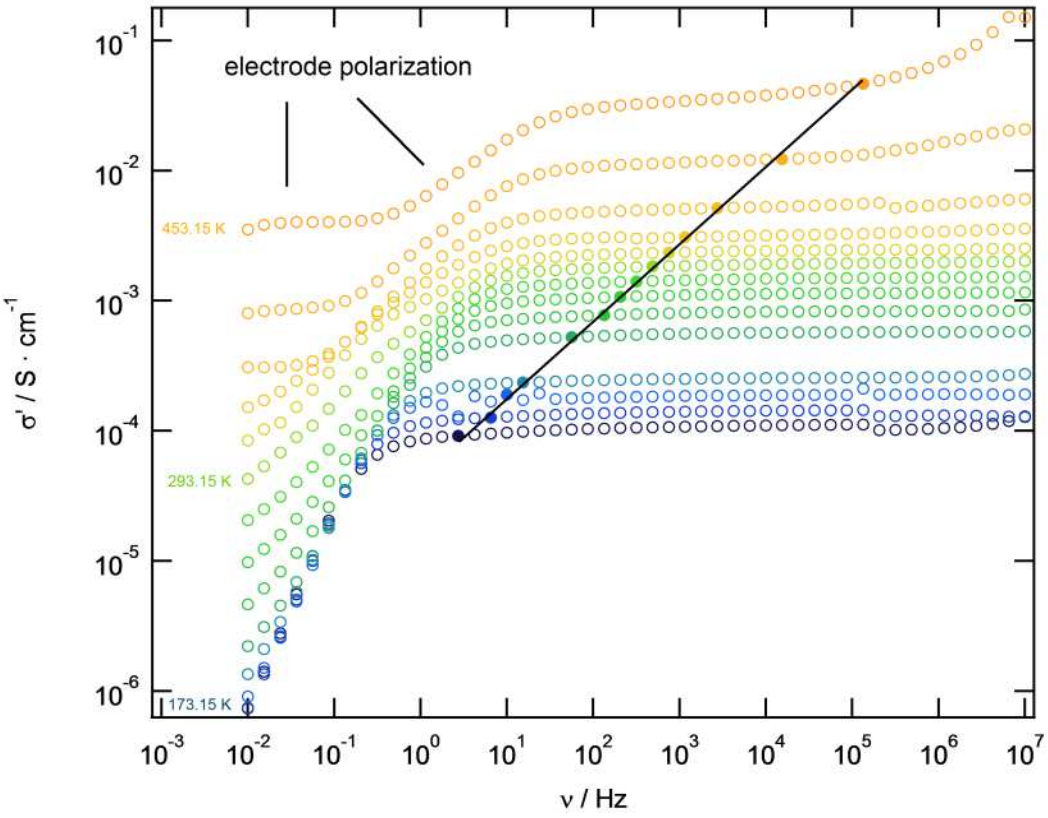

Figure 28: Conductivity isotherms of β-Ag_3SI at a frequency range from 10 mHz to 10 MHz and a temperature range from 173.15 K to 453.15 K. Between the isotherms of the highest temperatures (433.15 K and 453.15 K) a difference can be clearly seen. This difference may indicate a phase transformation.

Compared to lithium argyrodites, Ag_3SI has an even better conductivity. *β*-Ag_3SI reaches a conductivity at room temperature of $\sigma_{RT}=1.11\cdot10^{-3}$ S·cm^{-1}.

Again, by reading off the values of σ_{DC}, an Arrhenius plot was created. It is illustrated in Figure 29.

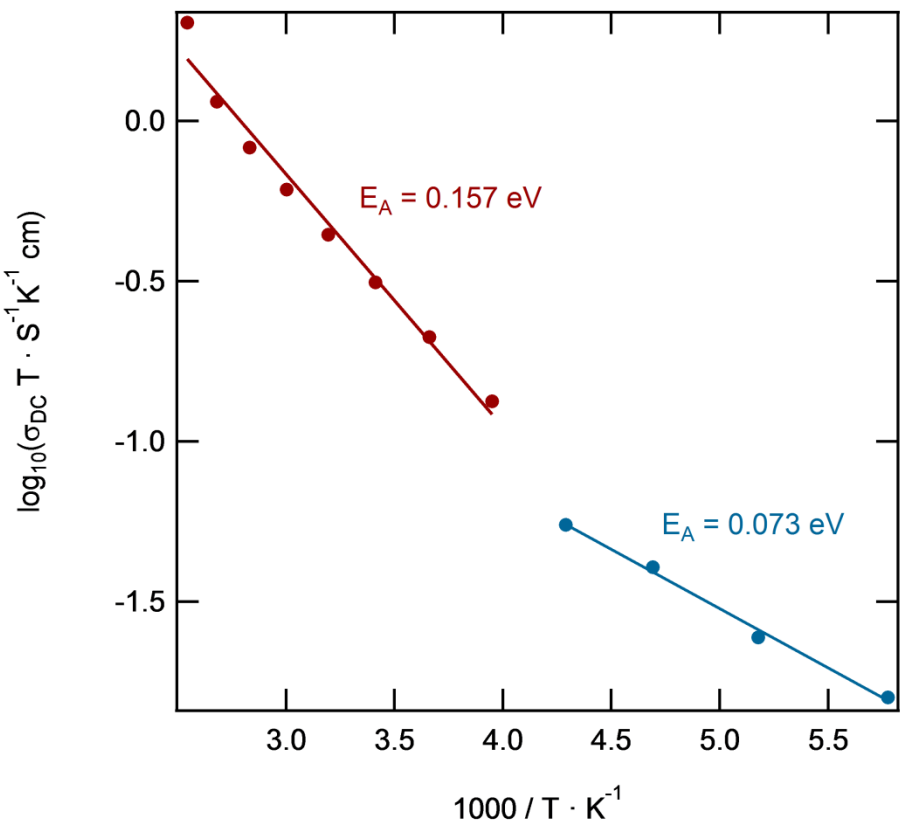

Figure 29: The Arrhenius plot shows the change of σ as a function of inverse temperature of β-Ag_3SI.

Two different activation energies can be calculated for β-Ag_3SI. This means that two different jumps or two different phases can occur within this structure.

In comparison to all other sulfide ionic conductors, which were synthesized and characterized during this work, the silver antiperovskite β-Ag_3SI has the lowest values. Activation energies of 0.157 eV and 0.073 eV were reached for the β-Ag_3SI. The mean activation energies are required for a successful jump at every heating and cooling cycle. Therefore a lower E_A-value means that a successful jump takes place more easily and the ionic conductor is higher conductive.

4.4 Antiperovskite Li_3SI

The following chapters describe the sample characterization via X-ray powder diffraction and impedance spectroscopy of the antiperovskite Li_3SI.

4.4.1 Sample characterization via X-ray powder diffraction

In Figure 30 the XRPD patterns of the antiperovskites Li_3SI with different preparation methods are represented.

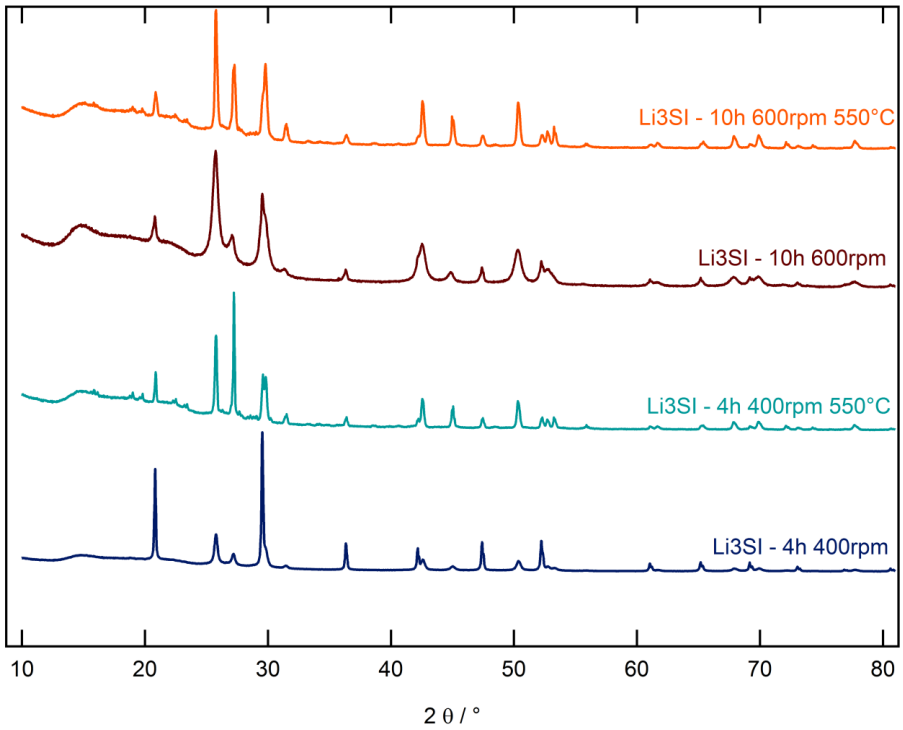

Figure 30: XRPD pattern of the antiperovskite Li_3SI at different milling times. The turquoise and orange reflections were also annealed at 550 °C.

In the XRPD patterns it is apparent, that a higher milling time does affect on the structure of the antiperovskite. The amorphous nature seems to increase with higher milling time, which is most likely induced by mechanical shear forces which affects the crystallinity of the sample during the milling process. Another effect of the higher milling time can be found in the reflection broadening, which can also be an indication for the reduction of crystallite size.

In the lattice parameters of the Li_3SI-structures, which are summarized in Table 10, differences are hardly recognized. That shows that the preparation process does not have much influence on the synthesis product of the solid-state reaction.

Table 10: Lattice parameter of the different prepared Li_3SI-antiperovskite samples.

Sample Li_3SI

Milling time / h	Rotations per minute / rpm	Annealing temperature / °C	Lattice parameter / Å
4	400	-	4.302
4	400	550	4.302
10	600	-	4.312
10	600	550	4.300

The two antiperovskite structures β-Ag_3SI and β-Li_3SI are similar.

In Figure 31 the general crystal structure of the lithium antiperovskite β-Li_3SI is illustrated.

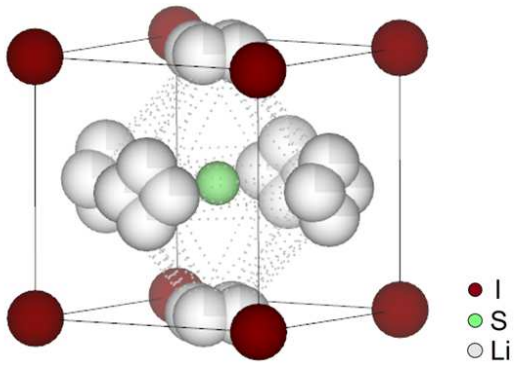

Figure 31: General crystal structure of the cubic β-Li_3SI antiperovskite.

The structure shows that the cubic *β*-Ag_3SI structure has a direct gap at M=(1/2, 1/2, 0), while the low-temperature *γ*-Ag_3SI has an indirect gap from M to Γ=(0, 0, 0) [29].

4.4.2 Sample characterization via impedance spectroscopy

Conductivity measurements of the lithium antiperovskite Li_3SI were again studied by means of electrochemical impedance spectroscopy. In the following, results of the milled (4 h, 400 rpm) antiperovskite are represented as a representative example for the conductivity studies performed on the various prepared sample. For the sample Li_3SI milled for 10 h at 600 rpm, no conductivity- and E_A-calculation was possible, because the pellet broke during the measurement.

For the conductivity measurement the obtained data are illustrates again in form of conductivity isotherms (see Figure 32).

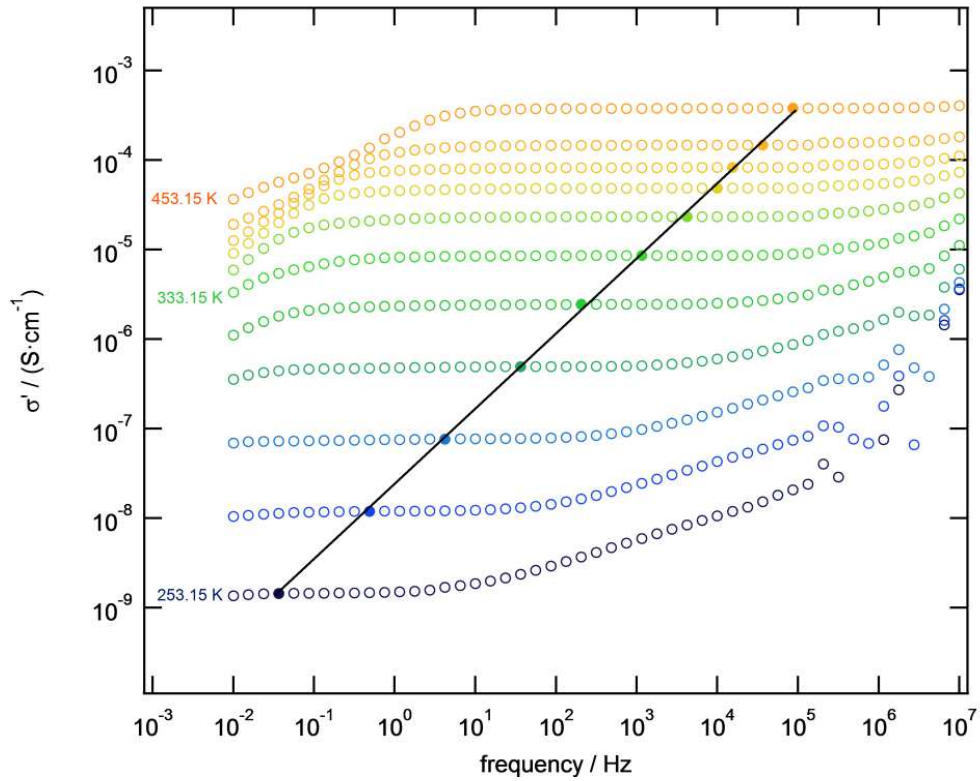

Figure 32: Conductivity isotherms of β-Li_3SI at a frequency range from 10 mHz to 10 MHz and a temperature range from 253.15 K to 453.15 K.

The conductivities of the various prepared samples are summarized in Table 11.

Table 11: Calculated conductivities σ_{RT} / Scm^{-1} of β-Li_3SI.

Sample β-Li_3SI

Milling time / h	Rotations per minute / rpm	Annealing temperature / °C	σ_{RT} / $S \cdot cm^{-1}$
4	400	-	$1.058 \cdot 10^{-7}$
4	400	550	$7.826 \cdot 10^{-7}$
10	600	550	$8.650 \cdot 10^{-9}$

Gained from the σ_{DC} values of the conductivity isotherms at every temperature the Arrhenius plot was pictured (see Figure 33).

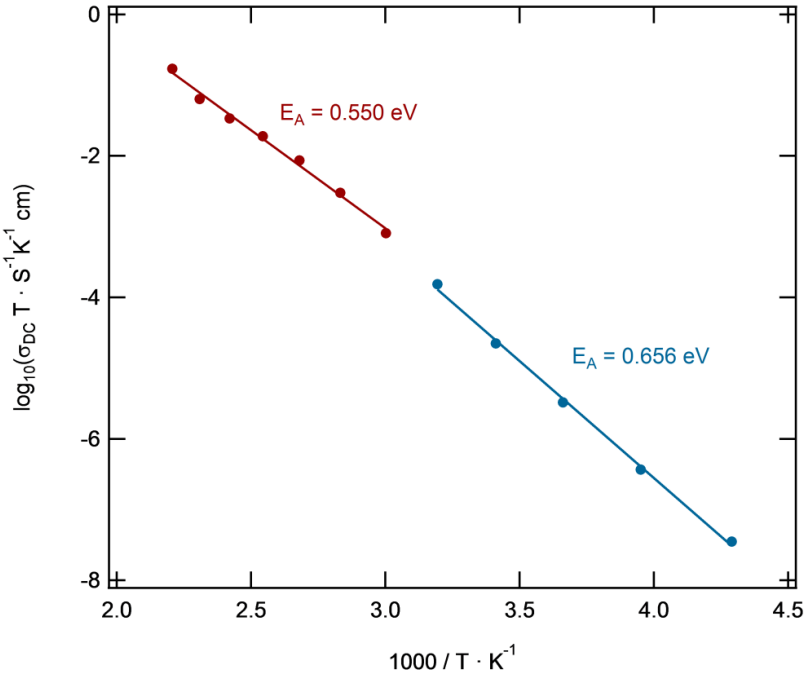

Figure 33: The Arrhenius plot shows the change of σ as a function of inverse temperature of β-Li_3SI.

Two different activation energies occur in sample Li_3SI, therefore two processes or a phase transition take place. The antiperovskite with silver Ag_3SI also showed two occurring processes.

Compared to β-Ag_3SI the activation energies are by a multiple higher. This means that more energy for a successful jump is needed. In Table 13 all calculated activation energies of β-Li_3SI are listed.

Table 12: Calculated activation energies [eV] of β-Li_3SI.

Sample β-Li_3SI

Milling time / h	Rotations per minute / rpm	Annealing temperature / °C	E_A / eV
4	400	-	0.65(6) and 0.55(0)
4	400	550	0.61(4)
10	600	550	0.61(5)

The activation energy of the sample that was not annealed shows a slightly higher value compared to the annealed samples. This is due to the annealing process. The grain boundaries are more defined by this process. Therefore, less energy is needed for a successful jump of the ion.

Finally, it must be noted that the β-phase lithium antiperovskite is very sensitive from a mechanical point of view and therefore the conductivity measurements could only be carried out to a limited extent.

5 Conclusion

In this work various sulfide ionic conductors, namely argyrodites with the formula Li_6PS_5X and antiperovskites with the formula Ag_3SI and Li_3SI were successfully synthesized via mechanical milling. Phases and structural properties were investigated by X-ray powder diffraction. The ion conductivity was carried out by electrochemical impedance spectroscopy.

For the lithium argyrodites both, XRPD and EIS showed that the influence of halogen atoms on the local environment plays an important role in Li^+-ion diffusion. The difference in Li^+-ion conductivity between Li_6PS_5Cl and Li_6PS_5I, which is several orders of magnitude, is caused by the distribution of the halogen ions across the available crystallographic centers. This suggests that changing the halogen distribution in lithium argyrodites during synthesis may increase the Li^+-ion conductivity of these sulfide ionic conductors.

To compare the Li^+-ion conductivities lithium argyrodite samples with fluorine-doped lithium argyrodite samples it is evident, that both sample-types show conductivities in the same magnitude. But there is a difference in activation energy. The activation energy of Li_6PS_5I is 0.470 eV. If the sample is doped with 5 % fluorine-content the activation energy decreases to 0.398 eV.

Additionally, for a better understanding of the effect of lithium-doping with fluorine a scanning electron microscopy (SEM) could be carried out, to determine the relative elemental concentration at a defined position of each element in the sample.

To stabilize the β-phase of the antiperovskites Ag_3Si and Li_3SI the samples were slowly cooled down (from 550 °C to 220 °C) and kept at 220 °C for two more days. The XRPD patterns also showed that a higher milling time does affect on the structural properties of the antiperovskite.

Finally, the silver antiperovskite β-Ag_3SI has proven to be the best synthesized sulfide ionic conductor in this work. It shows the best ion conductivity at room temperature with a value of $1 \cdot 10^{-3}$ $S \cdot cm^{-1}$ and an activation energy of 0.157 eV.

A. Appendix

Table A.1: Composition of lithium argyrodites (values in g)

	$Li_6PS_5Br_{0.75}Cl_{0.25}$	$Li_6PS_5Br_{0.25}Cl_{0.75}$	$Li_6PS_5Br_{0.75}I_{0.25}$	$Li_6PS_5Br_{0.25}I_{0.75}$
Li_2S	1.9048	2.0581	1.7696	1.6511
P_2S_5	1.8441	1.9899	1.7130	1.5969
LiBr	1.0816	0.3913	1.0042	0.3118
LiCl	0.1754	0.5690	-	-
LiI	-	-	0.5162	1.4419

Table A.2: Composition of the fluorine doped lithium argyrodites $Li_6PS_5Cl_{0.95}F_{0.05}$, $Li_6PS_5I_{0.95}F_{0.05}$ and $Li_6PS_5Br_{0.95}F_{0.05}$ (values in g)

	$Li_6PS_5Cl_{0.95}F_{0.05}$	$Li_6PS_5I_{0.95}F_{0.05}$	$Li_6PS_5Br_{0.95}F_{0.05}$
Li_2S	2.1479	1.6216	1.8539
P_2S_5	2.0769	1.5684	1.7941
LiCl	0.7527	-	-
LiI	-	1.7936	-
LiBr	-	-	1.3314
LiF	0.0244	0.0191	0.0213

Table A.3: Composition of the fluorine doped lithium argyrodites $Li_6PS_5I_{0.85}F_{0.15}$ and $Li_6PS_5I_{0.50}F_{0.50}$ (values in g)

	$Li_6PS_5I_{0.85}F_{0.15}$	$Li_6PS_5Br_{0.50}F_{0.50}$
Li_2S	1.6718	1.8778
P_2S_5	1.6172	1.8172
LiI	1.6552	1.0942
LiF	0.0566	0.2130

Table A.4: Composition of the antiperovskite Ag_3SI (values in g)

	Ag_3SI
AgI	2.4324
Ag_2S	2.5670

Table A.5: Composition of the antiperovskite Li_3SI (values in g)

	Li_3SI
LiI	3.7229
Li_2S	1.2781

6 Bibliography

6.1 References

[1] A. Hayashi, A. Sakuda, and M. Tatsumisago, “Development of Sulfide Solid Electrolytes and Interface Formation Processes for Bulk-Type All-Solid-State Li and Na Batteries,” *Front. Energy Res.*, vol. 4, no. July, pp. 1–13, 2016.

[2] M. Tatsumisago, M. Nagao, and A. Hayashi, “Recent development of sulfide solid electrolytes and interfacial modification for all-solid-state rechargeable lithium batteries,” *J. Asian Ceram. Soc.*, vol. 1, no. 1, pp. 17–25, 2013.

[3] A. R. West, *Solid State Chemistry and its Applications*. John Wiley & Sons, 2014, 2014.

[4] C. Suryanarayana, “Mechanical alloying and milling,” *Prog. Mater. Sci.*, vol. 46, no. 1–2, pp. 1–184, Jan. 2001.

[5] D. L. Johnson, “Solid-State Sintering,” *Ultrafine-Grain Ceram.*, pp. 173–183, 1970.

[6] Borg, R.J., Dienes, and D.J., *An Introduction to Solid State Diffusion.* San Diego: Academic Press, 1988.

[7] Mehrer Helmut, *Diffusion in Solids: Fundamentals, Methods, Materials, Diffusion-Controlled Processes*. Springer Science & Business Media, 2007.

[8] R. Bott, “Chemistry - General - Principles, Patterns & Applications,” *Igarss 2014*, no. 1, pp. 1–5, 2014.

[9] P. Averill, Bruce A; Eldredge, “Principles of General Chemistry,” in *Principles of General Chemistry*, 2012.

[10] E. Barsoukov and J. R. Macdonald, *Impedance Spectroscopy: Theory, Experiment, and Applications*. John Wiley & Sons, 2018.

[11] F. Preishuber-Pflügl and M. Wilkening, “Mechanochemically synthesized fluorides: Local structures and ion transport,” *Dalt. Trans.*, vol. 45, no. 21, pp. 8675–8687, 2016.

[12] P. Padma Kumar and S. Yashonath, “Ionic conduction in the solid state,” *J. Chem. Sci.*, vol. 118, no. 1, pp. 135–154, 2006.

[13] S. Baskaran, “Structure and Regulation of Yeast Glycogen Synthase,” no. August, 2010.

[14] Rudolf Gross and Achim Marx, *Festkörperphysik*, 2nd editio. Berlin/Boston: Walter de Gruyter GmbH, 2014.

[15] M. Ermrich and D. Opper, *X-RAY POWDER DIFFRACTION: XRD for the analyst*, 2013.

[16] H. M. Chen, C. Maohua, and S. Adams, “Stability and ionic mobility in argyrodite-related lithium-ion solid electrolytes,” *Phys. Chem. Chem. Phys.*, vol. 17, no. 25, pp. 16494–16506, 2015.

[17] J. Auvergniot, A. Cassel, J.-B. Ledeuil, V. Viallet, V. Seznec, and R. Dedryvère, “Interface Stability of Argyrodite Li6PS5Cl toward LiCoO2, LiNi1/3Co1/3Mn1/3O2, and LiMn2O4 in Bulk All-Solid-State Batteries,” *Chem. Mater.*, vol. 29, no. 9, pp. 3883–3890, May 2017.

[18] M. Clugston and R. Flemming, “Advanced chemistry,” *Oxford University Press*, 2000.

[19] Q. Zhou, Z. Fang, J. Li, and M. Wang, “Applications of TiO2 nanotube arrays in environmental and energy fields: A review,” *Microporous Mesoporous Mater.*, vol. 202, pp. 22–35, 2015.

[20] S. V. Krivovichev, “Minerals with antiperovskite structure: A review,” *Zeitschrift fur Krist.*, vol. 223, no. 1–2, pp. 109–113, 2008.

[21] K. Chen, C. Li, M. Hu, X. Hou, C. Li, and Z. Chen, “Deformation modes and anisotropy of anti-perovskite Ti3AN (A = Al, In and Tl) from first-principle calculations,” *Materials (Basel).*, vol. 10, no. 4, 2017.

[22] Shannon R.D., *Acta Cryst. A32*, 1976.

[23] M. A. Kraft *et al.*, “Influence of Lattice Polarizability on the Ionic Conductivity in the Lithium Superionic Argyrodites Li 6 PS 5 X (X = Cl, Br, I),” *J. Am. Chem. Soc.*, vol. 139, no. 31, pp. 10909–10918, Aug. 2017.

[24] P. Pct and V. Internationale, “Wo 2009/047254 a9,” no. 12, 2009.

[25] R. Metselaar and G. Oversluizen, “The meyer-neldel rule in semiconductors,” *J. Solid State Chem.*, vol. 55, no. 3, pp. 320–326, 1984.

[26] A. West, J. Irvine, and D. Sinclair, “Electroceramics : Characterization by Impedance Spectroscopy,” *Adv. Mater.*, vol. 2, no. 3, pp. 132–138, 1990.

[27] S. Hull, D. A. Keen, N. J G Gardner, and W. Hayes, “The crystal structures of superionic Ag3SI,” *J. Phys. Condens. Matter*, vol. 13, 2001.

[28] M. Z. A. Munshi, *Handbook of Solid State Batteries and Capacitors*. WORLD SCIENTIFIC, 1995.

[29] W. Shimosaka, S. Kashida, and M. Kobayashi, “Electronic structure of Ag3SI,” *Solid State Ionics*, vol. 176, no. 3–4, pp. 349–355, 2005.

6.2 List of Figures

6.3 List of Tables